12-2016

Performance Characterization of Ceramic Matrix Composites through Uniaxial Monotonic Tensile Testing

Jóhannes Pétursson

PERFORMANCE CHARACTERIZATION OF CERAMIC MATRIX COMPOSITES THROUGH UNIAXIAL MONOTONIC TENSILE TESTING

A Thesis

Submitted to the Faculty

of

Embry-Riddle Aeronautical University

by

Jóhannes Pétursson

In Partial Fulfillment of the

Requirements for the Degree

of

Master of Science in Aerospace Engineering

December 2016

Embry-Riddle Aeronautical University

Daytona Beach, Florida

PERFORMANCE CHARACTERIZATION OF CERAMIC MATRIX COMPOSITES THROUGH UNIAXIAL MONOTONIC TENSILE TESTING

by

Jóhannes Pétursson

A Thesis prepared under the direction of the candidate's committee chairman, Dr. Luis Gonzalez, Department of Aerospace Engineering, and has been approved by the members of the thesis committee. It was submitted to the School of Graduate Studies and Research and was accepted in partial fulfillment of the requirements for the degree of Master of Science in Aerospace Engineering.

THESIS COMMITTEE

Chairman, Dr. Luis Gonzalez

Member, Dr. Daewon Kim

Member, Dr. Virginie Rollin

Graduate Program Coordinator, Dr. Magdy Attia — 9.14.2016 Date

Dean of College of Engineering, Dr. Maj Mirmirani — 10/18/16 Date

Vice Chancellor, Academic Support, Dr. Christopher Grant — 11/7/16 Date

ACKNOWLEDGMENTS

I have always said that engineering is a team sport. Even in the process of completing my individual thesis, there have been many people along the way on whom I have relied for moral, technical, and logistical support, and I give my thanks:

Dr. Luis Gonzalez for his direction and patience as my thesis advisor, and for getting our technical paper accepted into the 2015 CMCEE ceramics conference in Vancouver, BC.

Dr. Daewon Kim for allowing me use of his tensile machine and DAQ devices, and for serving on my advisory board.

Dr. Virginie Rollin for teaching me the foundations of failure analysis, and for serving on my advisory board.

Escape Dynamics, Incorporated for providing the test materials and giving me the opportunity to pursue a career in material science.

Michael Potash for his steady hands in soldering the instrumentation on the brass dummy loads.

Samaksh Behl and Taher Surti for assisting in the multi-channel DAQ setup for the alignment test.

Anna Lawlor, my fiancé, for her unwavering support and understanding through the late nights and the long hours.

Mr. and Mrs. Pétursson for my early foundation in engineering (read "Lego").

TABLE OF CONTENTS

Page

LIST OF TABLES

LIST OF FIGURES

Figure Page

SYMBOLS

A	cross-sectional area
F	force
l	length
l_0	initial length
ϵ	strain
σ	stress

ABBREVIATIONS

ASTM	American society for testing and materials
CFCC	continuous fiber reinforced ceramic
CMC	ceramic matrix composite
CVI	chemical vapor infiltration
MI	melt infiltration
MUT	material under test
PIP	polymer infiltration and pyrolysis
PyC	pyrolytic carbon
SSTO	single stage to orbit
VP-SEM	variable pressure scanning electron microscope

ABSTRACT

Pétursson, Jóhannes MSAE, Embry-Riddle Aeronautical University, December 2016. Performance Characterization of Ceramic Matrix Composites Through Uniaxial Monotonic Tensile Testing.

Ceramic matrix composite (CMC) samples were tested in order to characterize their mechanical performance and provide metrics for material process refinement and component design. Monotonic, uniaxial tensile testing of an uncoated carbon fiber reinforced silicon carbide ceramic at room temperature was performed following ASTM standard C1275 to measure ultimate tensile strength and elastic modulus. Equipment verification was carried out through alignment measurement with a gaged tensile specimen using ASTM E1012 to ensure the monotonic nature of the testing equipment. Tensile strength data was treated with Weibull statistical models to produce A and B-basis strength properties for design values.

An alternative area measurement method separate from the C1275 procedure was employed to account for internal material voids. Using cross-sectional photography and image analysis, voids were measured and subtracted from area measurements for more accurate strength calculations. Successful tests of 11 CMC samples produced a mean tensile strength of 111.1 megapascals (MPa) and an elastic modulus of 912.8 MPa. The A-basis for strength was 77.54 MPa and the B-basis was 95.37 MPa.

1. Introduction

The field of composites expands the envelope for advanced materials that, while extremely effective in some operating conditions, can be especially unsuited for others. A composite, or the merging of two or more components into a single functional entity, combines the strengths of its ingredients, producing a material with improved or very different attributes from those of its constituents. The service environments involved in space flight can be chemically and thermally hostile, especially within propulsion systems and during atmospheric reentry, and traditional materials may not meet the high performance demand these conditions impose. This demand necessitates the development of innovative materials that support safe operation and mission assurance in such conditions. Refractory metals are viable options when high strength and temperature resistance are needed, however their low corrosion and oxidation resistance, coupled with their high mass, makes them unfavorable options for applications such as launch system heat shielding. On the other hand, ceramic materials are well suited for these conditions, but their inherently low tensile strength makes them unsuitable unless they are amalgamated with a stronger material. Ceramic matrix composites (CMCs) meet this need by introducing strong, fibrous reinforcement into otherwise weak ceramic materials, so their useful properties can be utilized even for structural applications. As the space industry continues to seek re-usability and re-

duced mass budgets to make space operations more economically viable, the concept of a single stage to orbit (SSTO) spacecraft represents the pinnacle of these goals. In lieu of ablative heat shielding, ceramic matrix composite (CMC) materials offer arguably the best chance of producing multiple-use components for extreme conditions in spaceflight due to their excellent strength-to-weight ratio, chemical inertness, damage tolerance, and thermal resistance. These materials are complex and difficult to model computationally, so building the body of empirical data and deepening the understanding of their attributes are valuable for design purposes.

1.1 Ceramic Composite Structure

CMCs are constituently expressed as a continuous phase, or matrix, and a distributed phase, commonly referred to as the reinforcement (Chawla, 2003). The presence of a ceramic continuous phase, as opposed to a polymeric or metallic one, is the distinguishing feature of this material. With all composites, the structures of the reinforcement phase can manifest as particles, chopped fibers, continuous fibers, and laminates.

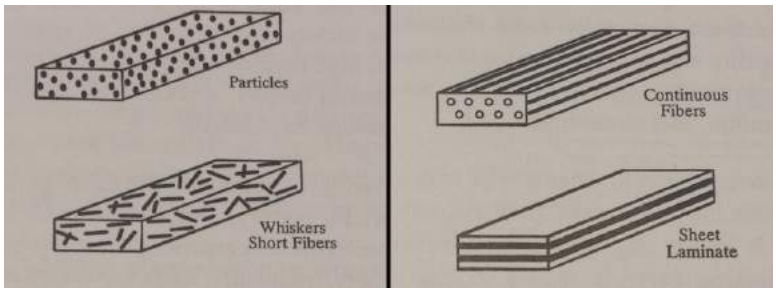

Figure 1.1. Types of reinforcements (Chawla, 2003).

The focus of this study is a continuous fiber-reinforced ceramic composite (CFCC) made up of carbon fiber and a silicon carbide matrix. For simplicity, this composite will be referred to in a fiber/matrix format as carbon/silicon carbide and abbreviated as C/SiC.

1.1.1 Fiber Preforms

A series of continuous fibers can be woven together in various patterns to form a laminate or even more complex 3-dimensional forms. The diameter of each carbon fiber filament is very small (on the order of 10 microns) so an individual strand, known as a tow, is actually a group of filaments usually numbering between 1 and 12 thousand, or 1k and 12k (Toray, 2015). These tows can support high loads in the direction of their fiber orientation and act as the primary structural member of the material. If the fiber reinforcement is discontinuous, like with particle and chopped fiber phases, the strength of the composite relies heavily on the strength of the interface between the reinforcement and the matrix. Since the reinforcement does not span the material, the matrix can fail around and between the reinforcements, causing complete fracture. Alternatively, if the fiber is continuous, matrix cracking can occur independently, while the continuous fiber and overall structure remains intact. However, since the fiber is only effective in the direction parallel to its orientation, its orthogonal strength is insubstantial compared to particles or randomly oriented chopped fibers (Ashbee, 1993). Layered CFCCs exemplify this problem, since the layers are held together with only matrix material. A load applied out-of-plane (through

the thickness of the material) will induce failure at a stress far below that of a fiber-parallel loading scenario, since almost all of the stress is applied to the matrix alone. In such a case, out-of-plane strength properties can be improved by using 3-D preforming techniques to weave orthogonal fibers through the laminate planes. While increasing manufacturing complexity and cost, these techniques introduce through-the-thickness fibers to the part, thus out-of-plane forces can be supported by fiber components

Woven Preforms

Mechanical properties of CMCs are very dependent on preform configuration. Even with an identical matrix, a uniaxial CFCC will behave very differently from a woven or braided CFCC. The reason for this is differing magnitudes of fiber crimping for different preforms. Crimp is inherent in most weaves and braids, and is generally defined as the amount an individual fiber strays from its centerline path, or what the fibers path would be if other fibers in the preform were not there to deflect it. Fiber crimp is inversely proportional to stiffness, because crimped fibers will tend to lengthen under tension due to the twisted fibers attempting to straighten themselves out (Stig, 2009). Additionally, crimped fibers exhibit reduced strength compared to straight fibers because their bends also induce flexural loads when tensed, compounding their stress state. These flexural forces induce a disproportional stress response to applied tensile force, therefore non-linearities in stress-strain curves of crimped preform CMCs are normal.

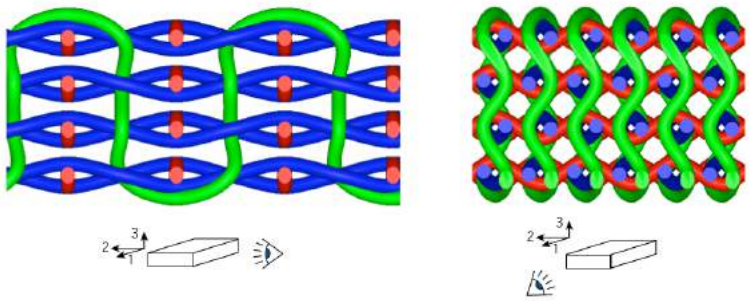

Figure 1.2. Planar views of a crimped 3D woven preform(Stig, 2009).

Non-Woven Preforms

In order to reduce the effects of crimping, 3-D orthogonal weaving was developed as a "zero-crimp" alternative to traditionally woven preforms. Figure 1.3 shows a 3-D weave in which no fiber has been pre-stressed because no fiber intertwines with any other. Theoretically, this eliminates crimp induced stress-strain non-linearity, and the CMC will behave similarly to a uniaxially reinforced composite under monotonic tension.

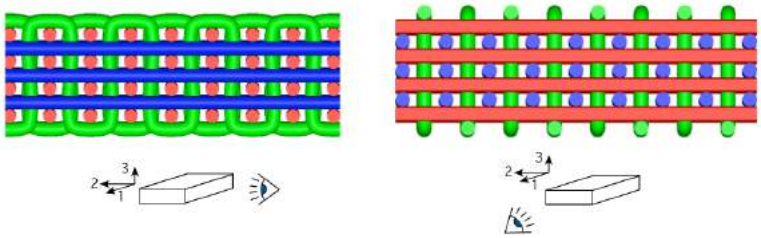

Figure 1.3. Planar views of a 3D non-woven preform (Stig, 2009).

1.1.2 Matrix Materials

Reinforcements like carbon fiber have high tensile strength. However, the filaments themselves are macroscopically weak and prone to fraying, and the fibers are slick and dissociate from their weave easily. Dispersive phases are used to infiltrate between fibers and filaments and harden in order to limit this undesirable dissociation. For aerospace, polymer and ceramic matrices are preferred over metal due to their lower density, but only ceramics can fulfill the ultrahigh temperature conditions of thermal rocket and reentry applications. Ceramics and polymers differ wildly in their material properties, most notably with their respectively brittle and ductile characteristics. A polymer matrix tends to have a low elastic modulus and high compliance around its encased reinforcement, while a ceramic one can be as stiff, if not stiffer, than its reinforcement and is more likely to crack than deform under stress (Krenkel, 2008). For this reason, the strong surface adherence between fiber and matrix inherent in polymer matrix composites (PMCs) can cause significant strength reduction when present in ceramic matrix composites. When the strain on a loaded CMC exceeds that which the matrix material can withstand, it will develop a crack that can cause a localized stress concentration on an adjacent fiber, leading it to fail at a lower load than its design load. This process is likely to propagate from the initial point of failure until local fiber fractures coalesce to the point of rapid, catastrophic failure of the part. In order to avoid this problem, the fibers can be coated with dissimilar

materials to promote slipping and remove or reduce the stress concentration created by the matrix crack.

Fiber Coatings

Matrix/fiber adherence is stronger in composites of similar constituent components, like a SiC/SiC CMC, because the chemical similarities between fiber and matrix predispose them to cohesion. The fiber coating that reduces this cohesion is known as an interfacial layer, and it is valued for more than just its mechanical effects. For high temperature applications, such coatings provide thermal protection and a chemically passive barrier for the fibers they contain. Some common interfacial materials with these attributes include boron nitride (BN), pyrolytic carbon (PyC), and SiC, although the latter would be a poor choice to improve slippage between SiC fiber and matrix.

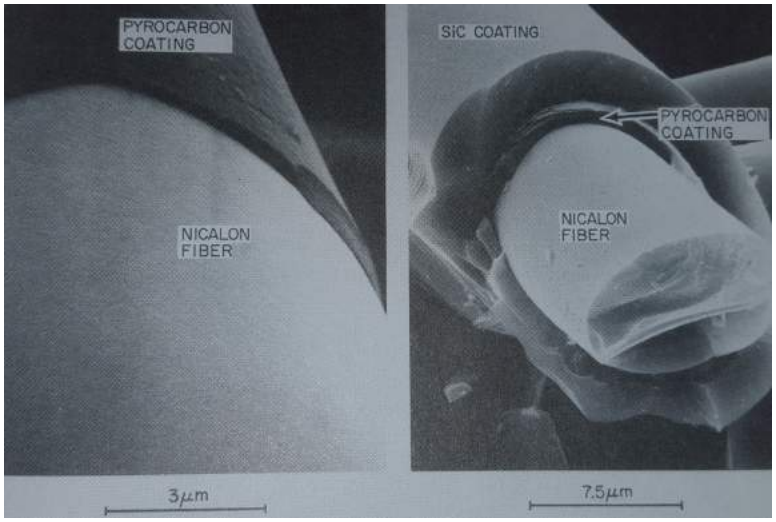

Figure 1.4. Interfacial layering of ceramic fibers (Chawla, 2003).

1.2 Processing Methods

One of the most involved aspects of CMC production is the processing of the matrix material to fully cure and encase the fiber reinforcement. Generally, the industry employs one of three methods, or a combination of them, for this purpose: melt infiltration, chemical vapor infiltration, and polymer infiltration and pyrolysis. A ceramic matrix will not cure sufficiently at room temperature, so all of the processing methods described require high temperature environments.

1.2.1 Melt Infiltration

Melt infiltration (MI) is the process of applying a liquid filler to a reactive substrate to form the desired matrix through chemical bonding. For example, a SiC matrix can be formed by introducing molten silicon into a carbon rich preform, whereby the free carbon and silicon react to form silicon carbide. This method is capable of producing a very dense matrix, in the sense that there are relatively few voids throughout the part due to imperfect or incomplete infiltration.

1.2.2 Chemical Vapor Infiltration

Chemical vapor infiltration (CVI) works by relying on gaseous decomposition on fiber surfaces for matrix formation. A carrier gas containing the matrix material is released into a confined space containing a substrate, in this case a fiber preform. The matrix material dissociates from the carrier gas and forms a solid upon contact

with the preform. This process is very slow, and does not result in an especially dense matrix due to airtight voids that form as a result of appreciable deposits of matrix on reinforcement fibers.

1.2.3 Polymer Infiltration and Pyrolysis

Polymer infiltration and pyrolysis (PIP) uses a liquid polymer precursor for wet layup of a fiber preform that is then processed at high temperature in an anaerobic environment, or pyrolyzed. Infiltration occurs during the liquid phase of the preceramic polymer, which, when heated, cross-links and out-gases the polymer components to leave a fully ceramic deposit. Densification is initially low, but repeated infiltration and pyrolysis over several cycles results in substantial matrix density of the final product.

1.3 Mechanical Testing of Ceramic Composites

Ideally, a ceramic composite with weak fiber/matrix bonding would exhibit strength characteristics in the fiber direction similar to those of the pure fiber reinforcement. In reality, many complicated factors contribute to strength properties of CMCs being lower than pure fiber, not least of which processing technique. In this case, the processing method of the samples used is preliminary, and the empirical characteristics of the current CMC test set will inform its iteration and refinement. For this study, material characterization efforts focus on determining elastic modulus and ultimate

tensile strength of flat, rectangular cross-section samples. These metrics provide a baseline for prototype component design, a comparison to theoretical models, and a foundation for tracking processing improvements.

1.3.1 CMC Testing Methods

There are multiple ways in which to obtain elastic modulus and ultimate strength data. Two loading regimes are available, tensile and flexural; each stressor has its own benefits and drawbacks to successful testing and data acquisition of flat CMC specimens. In either case, ASTM standards C1341 and C1275 for flexural and tensile testing, respectively, define the preferred procedures for variable isolation and repeatability for analysis of flat CFCC specimens.

Flexure Testing

The brittle, porous nature of these ceramics leads to poor survivability in active compression grip fixtures that are common with traditional tension machines. This is one of the main reasons that ceramic composites are often characterized with 3 and 4-point flexure tests, where the loading elements and are non-destructive (Figure 1.5).

The resulting stress state is not constant over the cross-section of the specimen, as the flexure results in tension on one side of the specimen and compression on the other. The resulting flexure strength data can be used to approximate tensile strength, but empirical evidence has shown that the ultimate strength gleaned from a flexural test

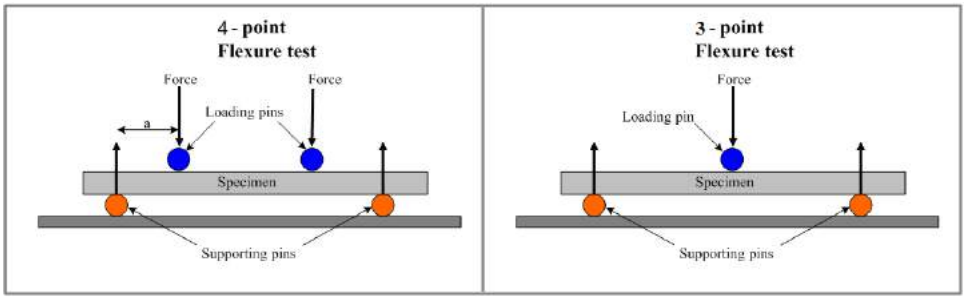

Figure 1.5. Load train diagrams of 4 and 3-Point flexure apparati (*Flexural Strength Tests of Ceramics*, 2012).

tends to be higher than that of a pure tension test (as much as a factor of 3 (Steif & Trojnacki, 1992)) for reasons that are categorically unquantified and unique to each specific material. This can make it difficult, especially with an anisotropic material, to correlate the measured bending strength to a tensile strength approximation with reasonable confidence. Additionally, this approximation assumes that the specimen has failed in tension. This is a reasonable assumption for materials with significantly higher compressive strength than tensile strength, but it is not one that can be easily made about the CMC material, whose matrix strength and density is unquantified.

Tensile Testing

Unlike flexural testing, tensile testing can produce a consistent cross-sectional stress state in a test sample by means of uniaxial loading. To prevent improper failure of ceramic composites in compression fixtures, metal tabs can be adhered to the ends of a test sample to provide a grip surface and distribute the fixture's

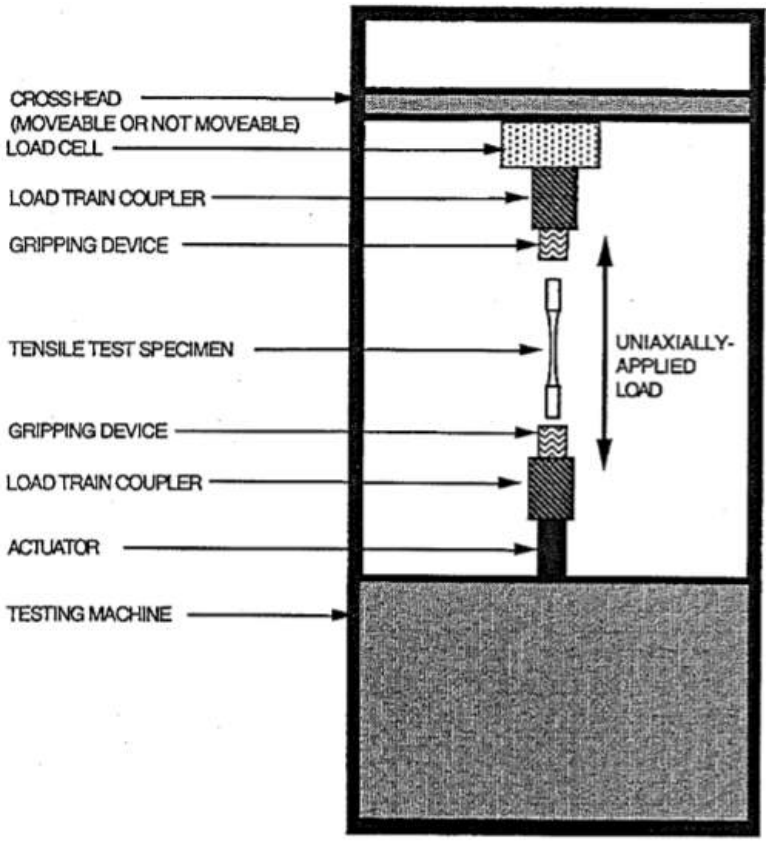

Figure 1.6. Load train diagram of uniaxial tensile apparatus (ASTM, 2014).

compressive force so the relatively fragile matrix within is not crushed. Unlike the relatively unconstrained loading condition of a flexural test fixture, the load train of a uniaxial tensile machine is prone to eccentric and angular misalignments which can apply undesired shear and moment forces to the sample (ASTM, 2014). Protocol C1275 advises verification of proper test apparatus alignment before carrying out testing using the E1012 procedure for load train alignment of tensile testing machines. Ultimately, this tensile method was chosen due to the uncertainty of its compression

strength, which needs to be high for a flexure test, and the greater confidence a pure stress state instills in the resulting strength data.

1.4 Failure Mechanisms for Ceramic Composites

Interfacial layering between fiber and matrix is commonplace in CMC manufacture, and so failure analysis tends to consider modes within this structural envelope. The tensile specimens under consideration for this study lack fiber coatings, and so the failure mechanics will differ with respect to the fiber and matrix interface. The constituents, however, are similar materials, so the fracture mechanisms of each employ the same failure theories.

1.4.1 Tensile Failure Mechanics of Ceramics

Ceramic materials are generally brittle and exceptionally strong in compression (Becker & Shipley, 2002), so their failure modes are almost exclusively due to tensile stresses with no ductility. Yet, ceramics rarely fail due to pure tension. Often times preexisting internal cracks lengthen under stress and propagate through the thickness of the material like in 1.7, heightening the stress state and inducing fracture.

Such fractures occur in two ways, relative to the self-contained crystalline structures known as grains that make up the material: intergranularly and intragranularly. Intergranular fracture indicates crack propagation that follows the paths between

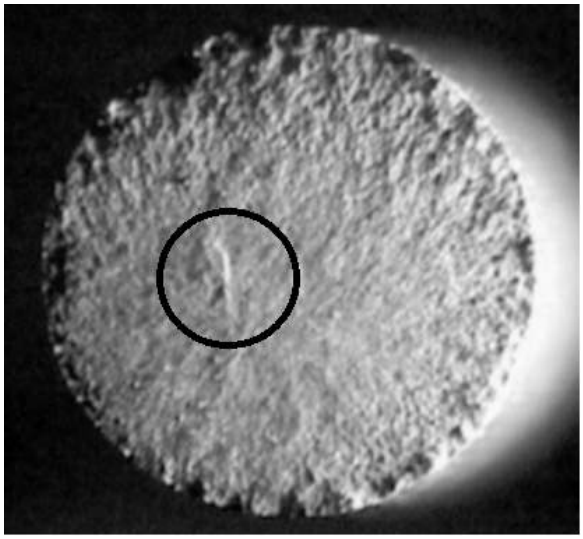

Figure 1.7. Fracture origin in silicon nitride rod under tension (Becker & Shipley, 2002).

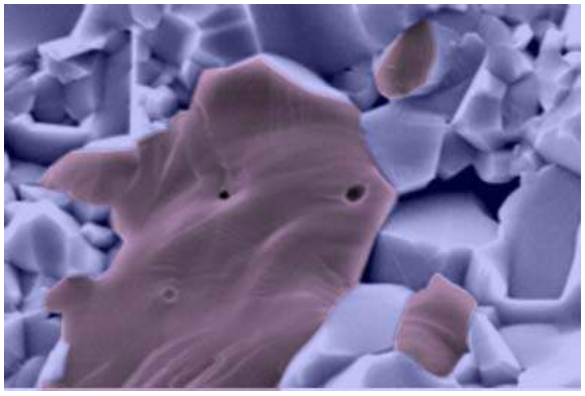

Figure 1.8. Interganular(blue) and intragranular(purple) fracture surfaces of polycrystalline alumina(Becker & Shipley, 2002).

grain boundaries. Intragranular fractures split through individual grains, and generally occur when grain boundaries are very strong.

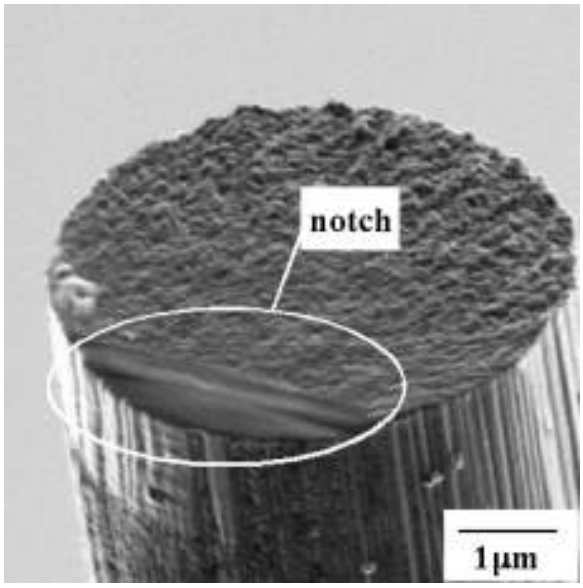

Figure 1.9. Brittle fracture behavior of notched carbon filament, similar to other ceramics (Ogihara et al., 2009).

Figure 1.8 shows a large grain split through, surrounded by intergranular cracks. While the topography of the intragranular crack is macroscopically smoother, ripples on the microscale identify the energetic behavior of the crack propagation through the grain. These ripples are not visible in intergranular cracks, providing a reliable way to distinguish between the two.

1.4.2 Failure Mechanisms of Coated Fibers

Since an interfacial fiber coating weakens the bonding strength between fiber and matrix, the ultimate CMC failure mode is fiber dominated. The brittle matrix can crack even at very low strains, so it is not uncommon for the fibers alone to constitute the only continuous load path through the material.

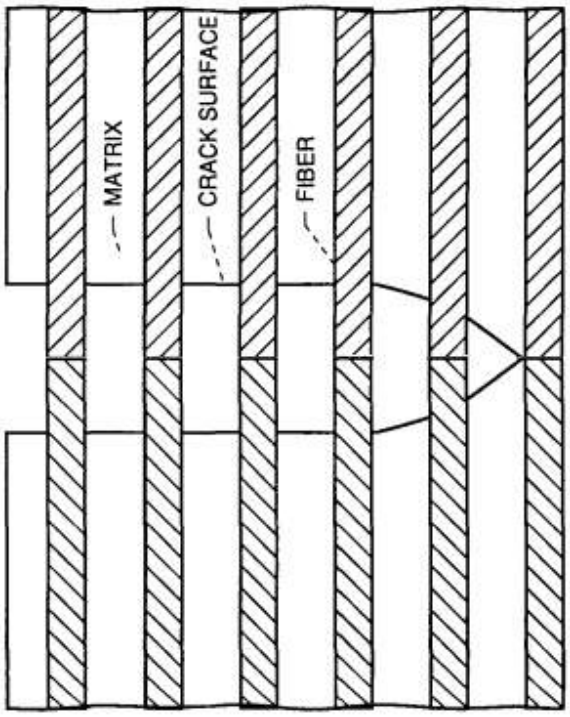

Figure 1.10. Matrix cracking and fiber slipping in a ceramic composite(Tripp et al., 1989).

As a result, the root cause of an individual fiber failure (Figure 1.9) is more likely internal imperfections than matrix-related stress concentrations. Thus, a fiber failure can occur somewhat randomly along its length, as demonstrated by Figure 1.11. This phenomenon is called "fiber pullout," (Figure 1.10) a hallmark of coated fiber systems.

Functional interfacial layers essentially eliminate matrix crack propagation as a primary failure mode. Instead, such systems fail progressively as individual fibers break until cumulative damage leads to complete fracture. Compared to unstable crack growth, which is fast and catastrophic, progressive failure modes are slow and "graceful," with audible snaps of individual fibers for early warning.

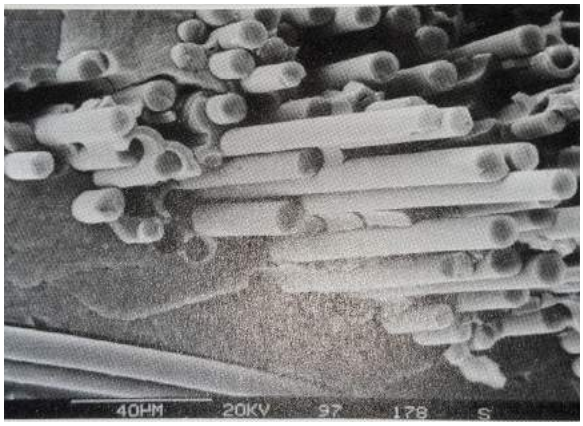

Figure 1.11. Fiber dominated fracture exhibited by high pullout (Krenkel, 2008).

1.4.3 Failure Mechanics of Uncoated Fibers

An uncoated fiber CMC failure will occur in the opposite manner. Upon cracking, the adhesive matrix locally stresses adjacent fibers, increasing the likelihood of the crack progressing through those fibers and into other matrix and fiber regions. Fracture is no longer graceful and fiber dominated, instead exhibiting similar crack propagation behavior to monolithic ceramics. Depending on the strength of fiber-to-matrix cohesion, the amount of fiber pullout at the fracture surface is minimal or absent, especially with identical materials like the SiC/SiC CMC pictured in Figure 1.12.

Different CMC systems may fall somewhere within the spectrum of these two extreme cases. An uncoated system with dissimilar components can still exhibit fiber pullout, and a defective or ineffective coating may allow matrix-dominated failure. Therefore, matrix-fiber cohesion should not be assumed based on composition alone.

Figure 1.12. Matrix (blue) dominated fracture of an uncoated SiC/SiC CMC exhibited by zero fiber pullout (purple) (Chawla, 2003).

1.5 Technical Objectives

It is the purpose of this thesis to utilize the information presented above to gather and synthesize mechanical properties of an uncoated PIP manufactured C/SiC CMC through destructive testing, and to perform post-test failure analysis upon its fracture surfaces for the purpose of component design and process refinement. Tensile testing using ASTM procedure C1275 will be used as the loading method to gather ultimate strength and elastic modulus data, and procedure E1012 will be followed to verify alignment of the load train. Qualitative failure analysis of the fracture surfaces will be performed with the use of electron microscopy.

2. Equipment Verification

Tensile testing machines are designed to apply uniaxial force to a test specimen. Nevertheless, they may become misaligned, applying off-axis forces to the test specimen. The load train of a tensile machine can be eccentric, angular, or a combination of the two (Figure 2.1, page 20), and it is important to ensure the extent of these misalignments are within acceptable levels before there can be confidence in the monotonic nature of the tensile test.

2.1 Alignment Test Procedure

The alignment test is performed with respect to the ASTM code of practice E1012 for the measurement of misalignment induced bending in uniaxially loaded tension-compression test pieces (Bressers, 1995). The test involves elastic deformation of a specimen with a minimum of 8 strain gages to calculate the induced bending from load train misalignment of the testing machine. The specimen under scrutiny is flat, which by protocol requires the gages be applied in the pattern visualized in Figure 2.2.

However, the CMC material is porous enough that strain gages cannot reliably adhere to its surface. Instead, an isotropic, homogenous alternative “dummy” mate-

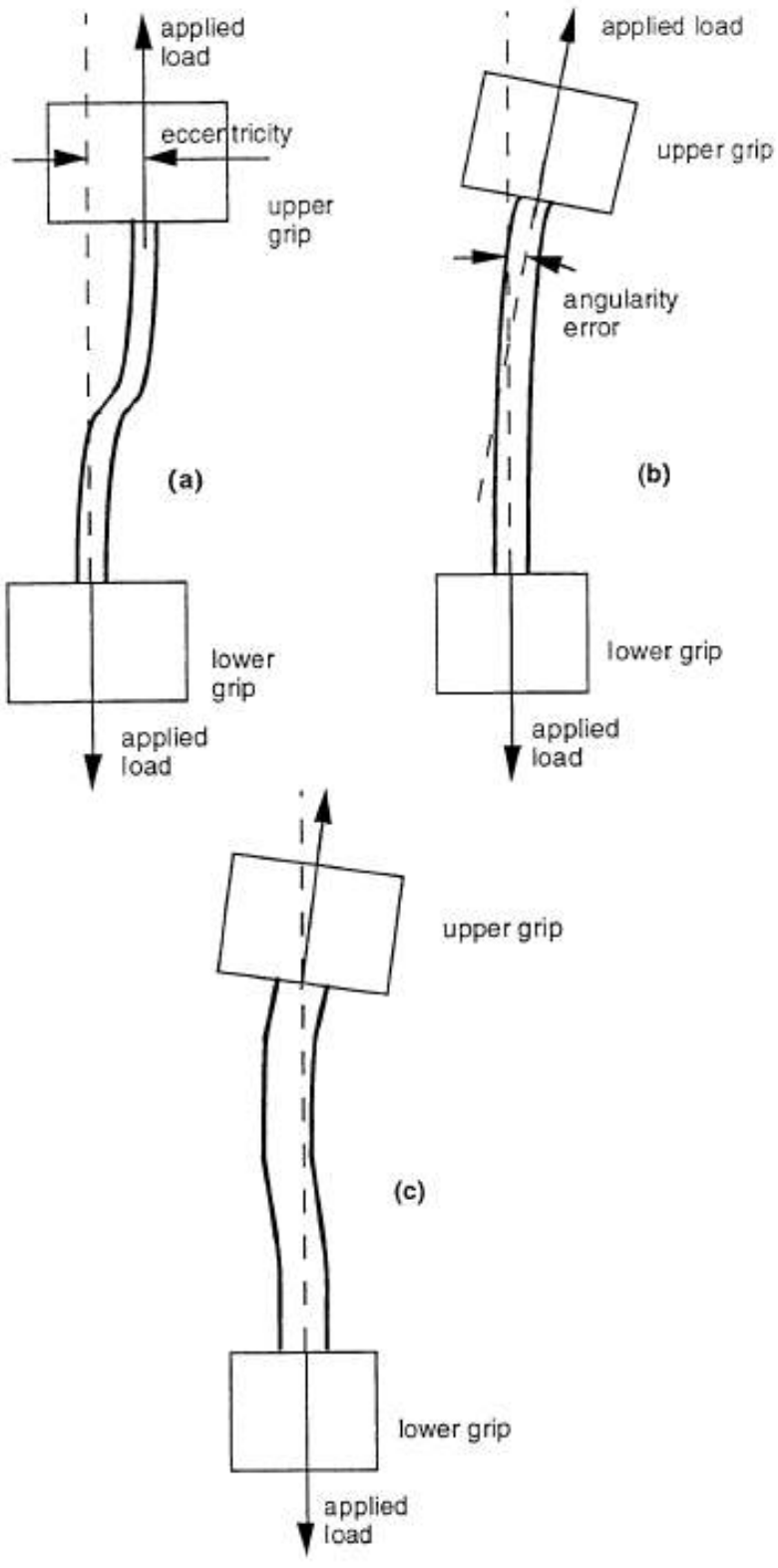

Schematic presentation of different sources of misalignment:
(a) concentricity error;
(b) angularity error;
(c) combination of (a) and (b).

Figure 2.1. Load train misalignment modes (Bressers, 1995).

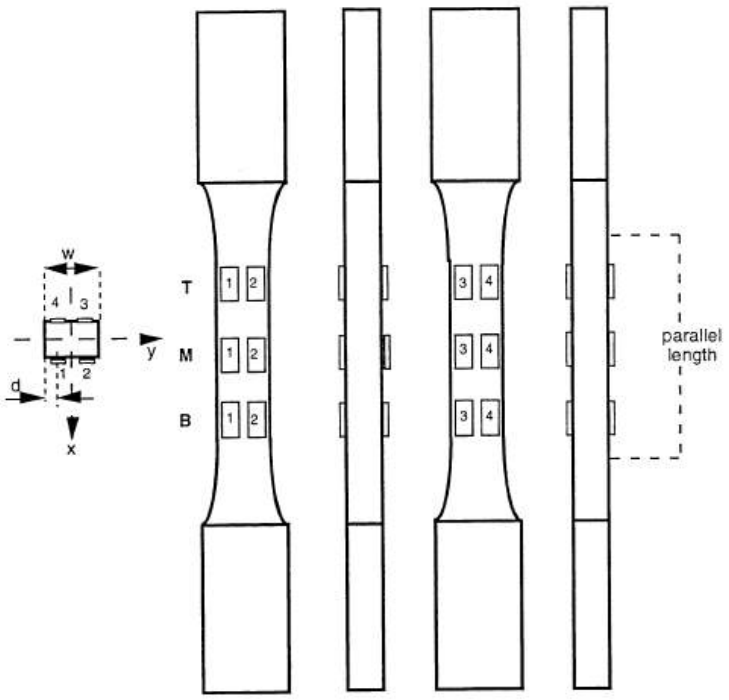

Figure 2.2. Flat specimen strain gaging (Bressers, 1995).

rial with similar elastic modulus and yield strength is used for more reliable results. Data from a similar CMC in Table 2.1 is used as a reference for such a material.

Brass alloy 385 is an analogous material with a yield strength and elastic modulus of 15,000 ksi and 14,000 ksi, respectively (McMaster-Carr, 2015) compared to the reference's 14,300 ksi and 15,900 ksi. This material has the added benefit of being easily machinable, which means it can be reliably cut to match the design shape (Figure 2.3) of the tensile specimen. The importance of this shape will be elucidated in a proceeding section titled "Specimen Preparation."

Table 2.1. C/SiC CMC properties (COI Ceramics, 2015).

Property	Value
Fiber Volume	40%
Bulk Density	2.1 g/cc
Tensile Strength	42 ksi
Tensile Modulus	15.9 Msi
Yield Stress	14.3 ksi
Strain to Failure	0.53%
Flexure Strength	35 ksi
Short Beam Shear Strength	4.0 ksi
Interlaminar Tensile Strength	800 psi

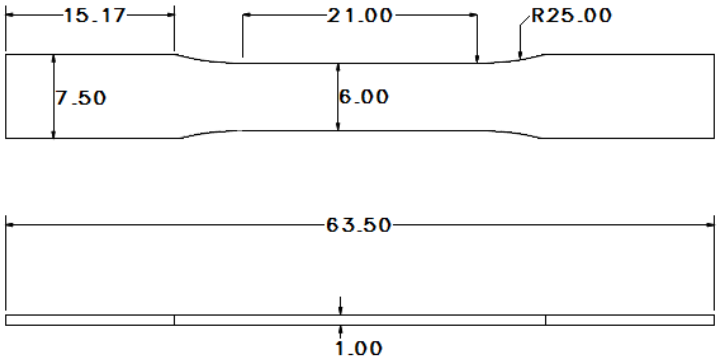

Figure 2.3. CMC tensile specimen dimensions.

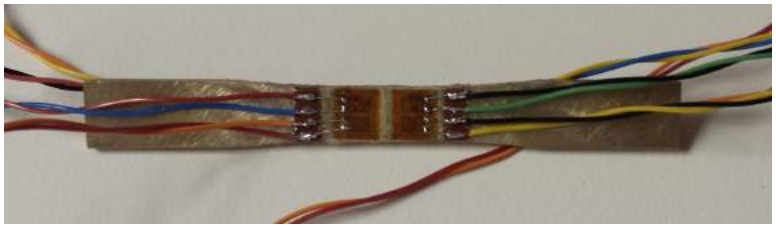

Figure 2.4. Brass specimen with strain gages.

The 8 strain gages are powered by an 8 channel signal conditioner with potentiometer screw terminals and a 16 channel DAQ connected to LabVIEW®. After placement in the testing machine, strain gage voltages are zeroed by hand using the potentiometer screws and allowed to settle for 30 minutes to reach pre-load equilibrium. The tensile load of the alignment test is specified as the maximum force applicable by the tensile machine or 75% of the limit of the elastic material, whichever is smaller.

$$F_{alignment} = 0.75 * E_{Brass} * A_{Brass}$$

$$F_{alignment} = 0.75 * (103.4MPa) * (6mm * 1mm)$$

$$F_{alignment} = 465.3N < F_{testing-machine} = 889.6N$$

Since the 75% elastic limit of 465.3N is smaller, it is the recommended force at which to measure misalignment. There was concern that the humid conditions of the dummy's pretest storage would degrade the strain gage adhesive, so this value was artificially lowered to 400N.

2.2 Alignment Test Results

After tensioning, all strain gages were allowed to equilibrate again for 30 minutes before voltage data was collected. The raw data was used to calculate percent bending based on proportional deviation from the mean.

Two tests were performed out of the 5 recommended by the alignment procedure. Two gages de-bonded from the specimen surface and were damaged in the attempt to reapply them. Time limitations prohibited the possibility of constructing a new specimen, preventing the completion of the prescribed number of tests. The two successful tests revealed bending values within the 5% bending threshold specified by protocol E1012 for all gages, suggesting misalignments inherent in the testing apparatus were within acceptable levels for CMC tensile testing to proceed.

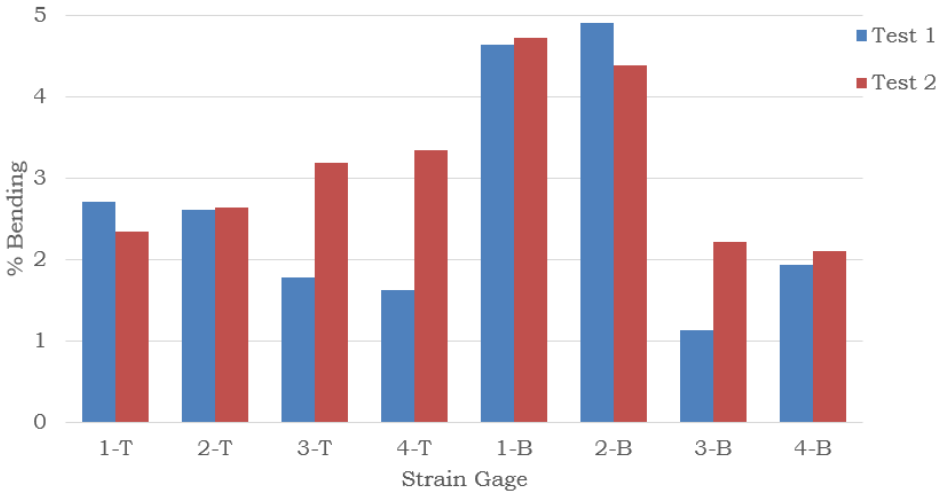

Figure 2.5. Percent bending of each strain gage.

3. Tensile Testing

The number of CMC samples available for tensile testing was limited. For this reason, maximizing the quantity and likelihood of successful tests is prioritized in the design of specimen shape and testing procedure. The experimental method described herein follows the ASTM procedure for monotonic tensile testing of a CFCC with a rectangular cross-section at room temperature, both in test setup and procedure. The only requirement deviation is that strain data was not gathered using either extensometers or strain gages. The former had prohibitive lead time and cost constraints due to the small size of the gage section, and the latter would have required using epoxy to adhere to the gage section, thereby altering the gage properties. The decision was made to prioritize ultimate tensile strength data over elastic modulus, requiring strain values to be calculated from displacement in order to protect the state of the gage section.

3.1 Specimen Preparation

For a test to be considered successful, a test sample must experience fracture within its gage section (ASTM, 2014), far from clamping surfaces or other foreign interfaces. To avoid crushing the specimen, space was allowed for aluminum tabs to be glued to the ends of the specimen using 5 minute set Loctite epoxy. The specimen

ends were designed with enough surface area for the shear strength of the epoxy to exceed the tensile strength of the reference CMC in Table 2.1.

The transition region to the gage section is smooth and gradual to avoid stress concentrations that may cause fracture within the region, resulting in a failed sample. A minimum transition radius of 50mm is recommended, but not required (ASTM, 2014); instead, the specimen was designed with a 25mm transition radius. The reason for this is some epoxy overflow is allowed at the sharp transition to the sample ends, adding to strength and crack resistance while increasing the size of the gage section and the likelihood of a fracture being localized within it. As mentioned before, the

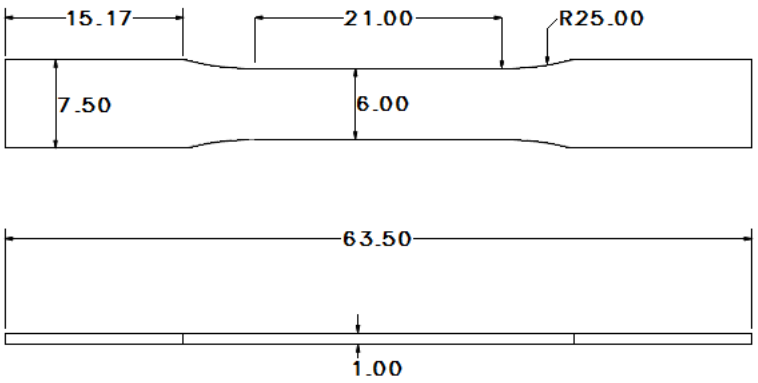

Figure 3.1. CMC tensile specimen dimensions.

width was determined by the strain gages used for the alignment test. Even though the ceramic specimens were not gaged, the same design must be used for the tensile test to maintain reasonable confidence in the load train alignment. To cut the CMC sample profiles, spare alignment specimens were used as stencils to profile the proper

dog-bone shape with a diamond coated rotary tool. 3 different 2.5 square parent coupons of C/SiC composite (designated as R252, R253, and R254) were cut to produce all 14 tensile specimens. An individual sample is referred to as R252-1, R252-2,..., R252-n, identifying the parent coupon and the nth sample produced from that coupon.

3.2 CMC Specimen Testing

With the CMC specimens cut and tabbed, a tensile loading program with a single ramp 10 mm/min displacement rate was applied to each specimen in order to achieve fracture within the ASTM recommended 5 to 10 seconds (discounting preload time) to minimize environmental effects on the sample (ASTM, 2014). Of 14 specimens tested, 11 successful fractures and 3 non-gage section fractures were documented; the data for the latter were discounted from further analysis.

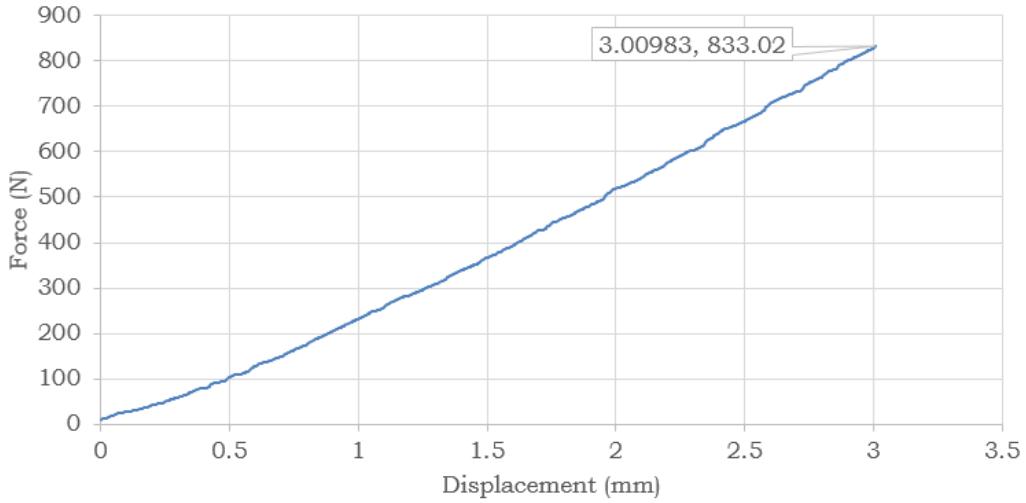

Figure 3.2. R252-1 force vs. displacement curve.

The testing machine is designed to collect force and grip displacement data from which stress or strain can be calculated if cross-sectional area or elongation, respectively, are known values. For cross-section measurement, a flat anvil micrometer is used to determine width and thickness of the specimen at three different locations along the gage section before testing. These values are then averaged to standardize the area across the full gage section of the sample.

Table 3.1. Specimen measurements.

	Width Measurements (mm)			Average Width	Thickness Measurements			Average Thickness	Mean Area (mm^2)
R252-1	5.94	5.90	5.85	5.91	1.23	1.21	1.25	1.23	7.25
R252-2	6.17	6.12	5.98	6.09	1.30	1.27	1.25	1.27	7.75
R252-3	6.03	5.88	6.09	6.00	1.46	1.52	1.35	1.44	8.66
R252-4	6.16	6.15	6.30	6.20	1.26	1.24	1.21	1.24	7.67
R253-1	5.87	5.94	6.02	5.94	1.38	1.37	1.36	1.37	8.14
R253-2	5.81	5.76	6.01	5.86	1.29	1.18	1.25	1.24	7.27
R253-4	6.01	5.90	6.00	5.97	1.23	1.24	1.26	1.24	7.42
R253-5	6.06	5.96	6.19	6.07	1.27	1.24	1.22	1.24	7.55
R254-2	5.56	5.72	5.66	5.65	1.26	1.20	1.19	1.22	6.87
R254-3	5.64	5.62	5.56	5.61	1.23	1.25	1.24	1.24	6.95
R254-4	5.36	5.74	5.81	5.64	1.25	1.22	1.20	1.22	6.90

In order to calculate elongation, only the original gage length dimension is used; the tabbed and tapered sections are not included. This length is used along with the testing machines load train displacement to determine the strain in the specimen. Strain data is extrapolated using the following equation:

$$\epsilon = (l - l_0)/l_0 \tag{3.1}$$

Where

$$l - l_0 = machine\ displacement \tag{3.2}$$

and

$$l_0 = 21mm \tag{3.3}$$

Using the mean cross-section area and force applied by the load train, stress is calculated with the equation

$$\sigma = F/A \tag{3.4}$$

The results are plotted on a stress vs. strain curve from which further material properties can be gathered.

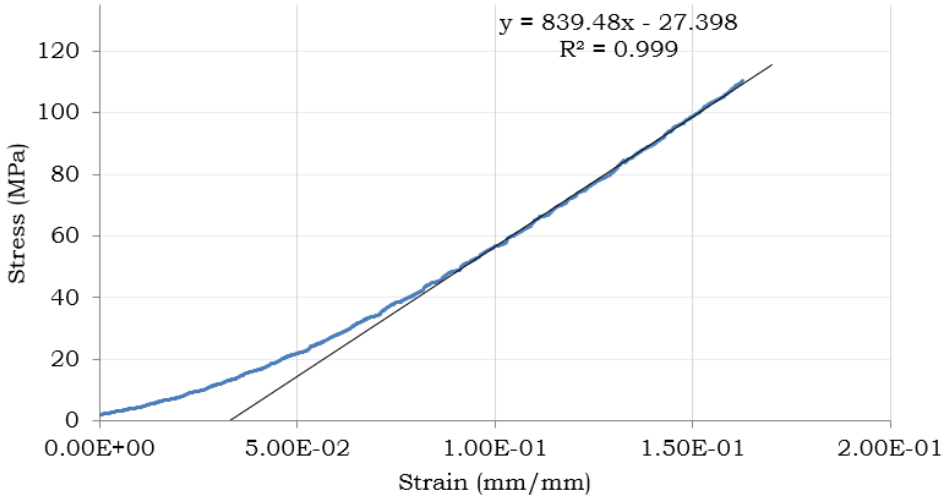

Figure 3.3. Stress-strain curve of fractured specimen R252-4.

There is some non-linearity on the graph due to straightening of the crimped fabric and the sample settling into the grips, so data regressions are assessed for the latter portion of the data where the graph has straightened. A linear fit is taken of the

stress vs. strain curve, and the slope of the trend line indicates the average modulus of elasticity of the material, which is recorded for all specimens in 3.4. Since only load train displacement was recorded, these measurements are significantly less accurate than they would be using more precise strain measurement tools.

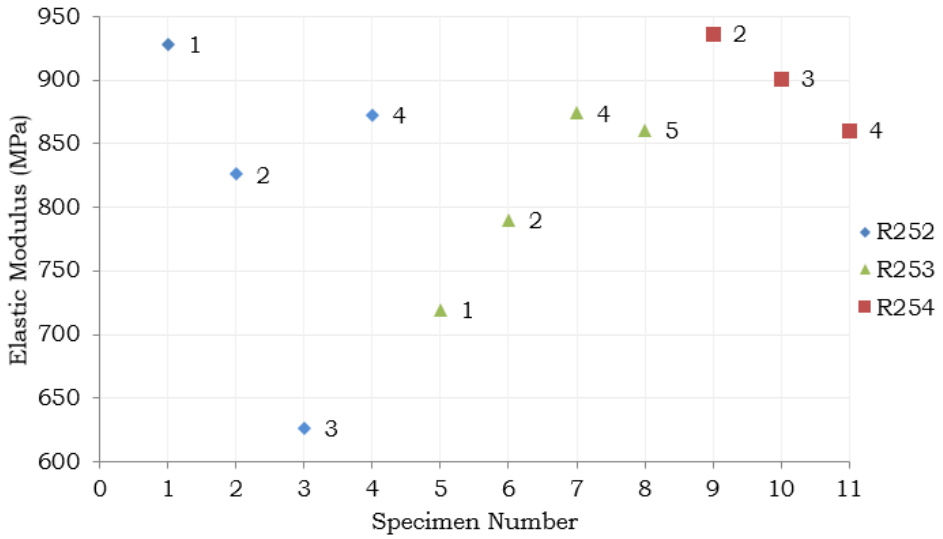

Figure 3.4. Elastic modulus of all specimens.

The tensile machine automatically truncates data after sample fracture, so the maximum stress and strain experienced by sample R252-4 are clearly visible. These data are tabulated with the linear fit data from the other 10 successful tests (Table 3.2). The measurement error propagations for tensile strength and fracture strain are then calculated and plotted with their respective sample data in Figures 3.5 and 3.6.

Table 3.2. Tensile material properties of successful specimens.

	Micrometer Measured Cross Sections		
	Elastic Modulus (MPa)	Ultimate Tensile Strength (MPa)	Fracture Strain %
R252-1	928.01	114.9	14.3
R252-2	826.03	108.9	16.8
R252-3	626.03	77.20	14.8
R252-4	872.28	110.2	16.3
R253-1	719.17	94.87	16.3
R253-2	789.8	96.72	16.3
R253-4	874.23	103.1	16.1
R253-5	860.52	111.6	17.6
R254-2	937.2	112.6	15.7
R254-3	901.72	102.6	15.0
R254-4	860.66	86.69	14.2
Average	853.97	101.8	15.8
St. Dev.	93.27	11.89	1.07

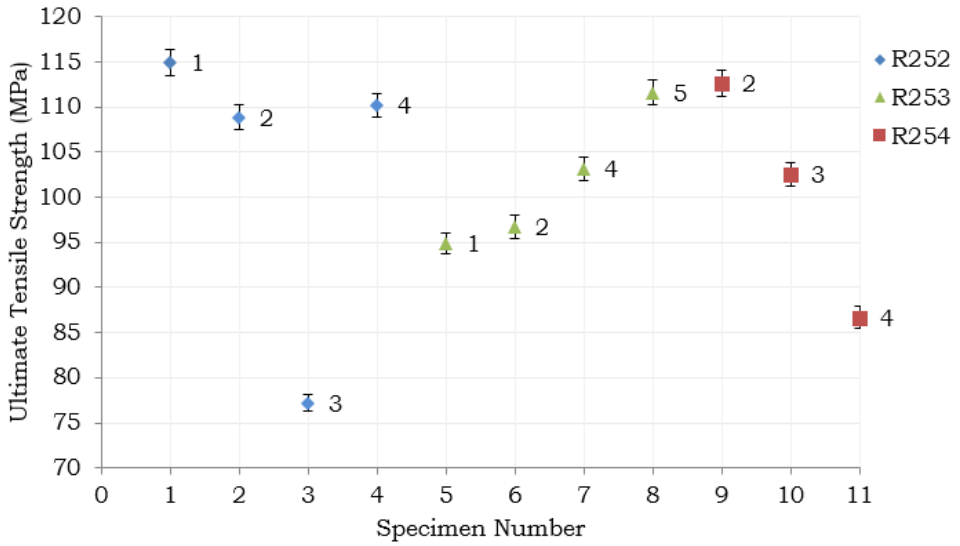

Figure 3.5. Ultimate tensile stress for all specimens, including measurement error propagation.

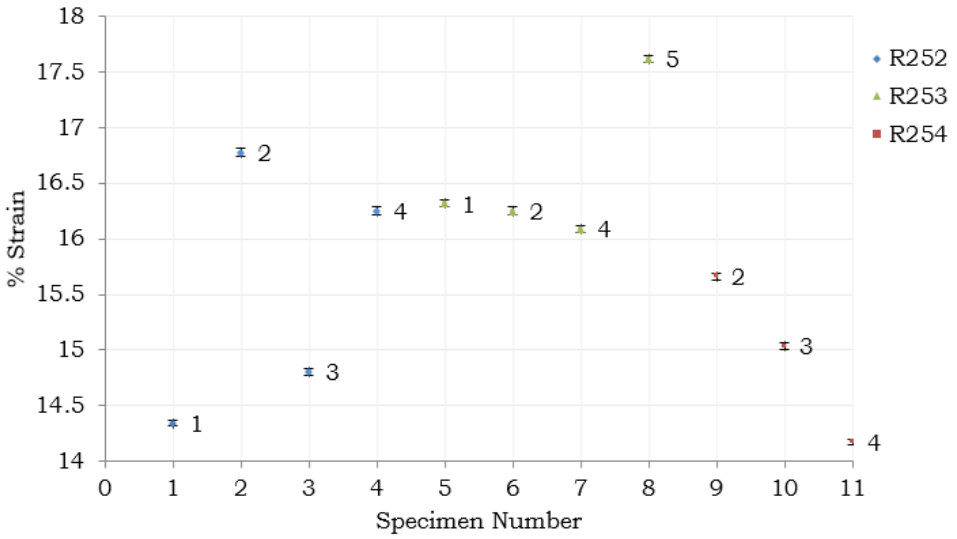

Figure 3.6. % Fracture strain for all specimens, including measurement error propogation.

The amount of variance in the values for each of the preceding parameters is substantial. This can be attributed to the variance inherent to ceramic materials, as well as the anisotropy of the material, with fiber volume differing somewhat between samples. This may indicate why the strength of R252-3 appears to be a low outlier, but was not discounted from testing since there were no testing abberations or samples anomalies detected. Also, troughs and voids in the cross section are not possible to measure with an anvil micrometer, so the property measurements likely reflect an overestimate of cross-section area. To explore this potential inaccuracy further, the same area can be measured with more elaborate tools during cross-section analysis. With appropriate microscopy equipment, the physical cross-section itself can be faced, photographed, then measured accurately with image analysis software.

3.3 Cross Section Analysis

This measurement technique relies on image analysis to make a pixel count of a cross-section image, relating those pixels to a reference object of known size, and converting the pixel count to an area measurement; a clear image is essential for this method's success. However, using post-fracture cross sectional measurements for stress calculations requires that the difference between true strain and engineering strain is small, or more specifically, that necking is not a significant failure mechanism that would alter the cross-section substantially. In the case of a C/SiC CMC, all materials involved are very brittle and the strain to failure of T300 carbon fiber is exceptionally low (1.5 percent (Toray, 2015)). Since necking can be eliminated as a failure mode, a post-fracture cross-sectional measurement will be as accurate as pre-test one. This fact is corroborated by the procedure allowing area measurements to be taken before or after testing (ASTM, 2014).

3.3.1 Cross Section Photography

After specimen fracture, one of the two fracture surfaces of each tensile specimen is faced with a cutting tool. The face is then oriented in a scanning electron microscope (SEM) chamber normal to the microscope aperture and photographed as in Figure 3.7. A short field of focus is beneficial for this process so only the cross-section surface is in focus.

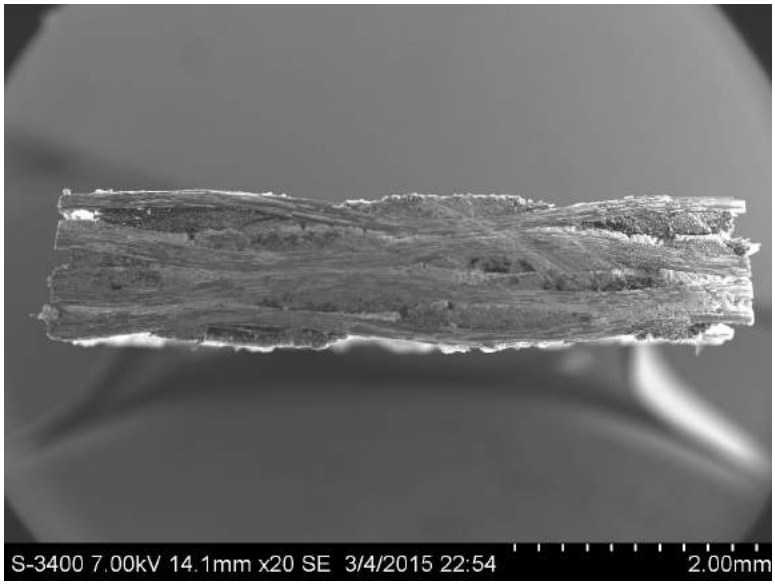

Figure 3.7. Cross section of R254-4.

3.3.2 Image Analysis

This photo is imported into image analysis software. A function executes the command to select only pixels in focus, which produces a contour around the selected pixels.

The total pixel count is calculated (Figure 3.8), but in order for this information to be useful as a physical measurement, a pixel count must be correlated directly to a known physical distance. The scale in the SEM image is approximate, and the SEM itself lacks a measurement feature. Instead, the micrometer data for the widest point of the cross section is borrowed for this method to provide a reference measurement. This reference distance provides a direct pixel to length conversion for area calculation (Table 3.3).

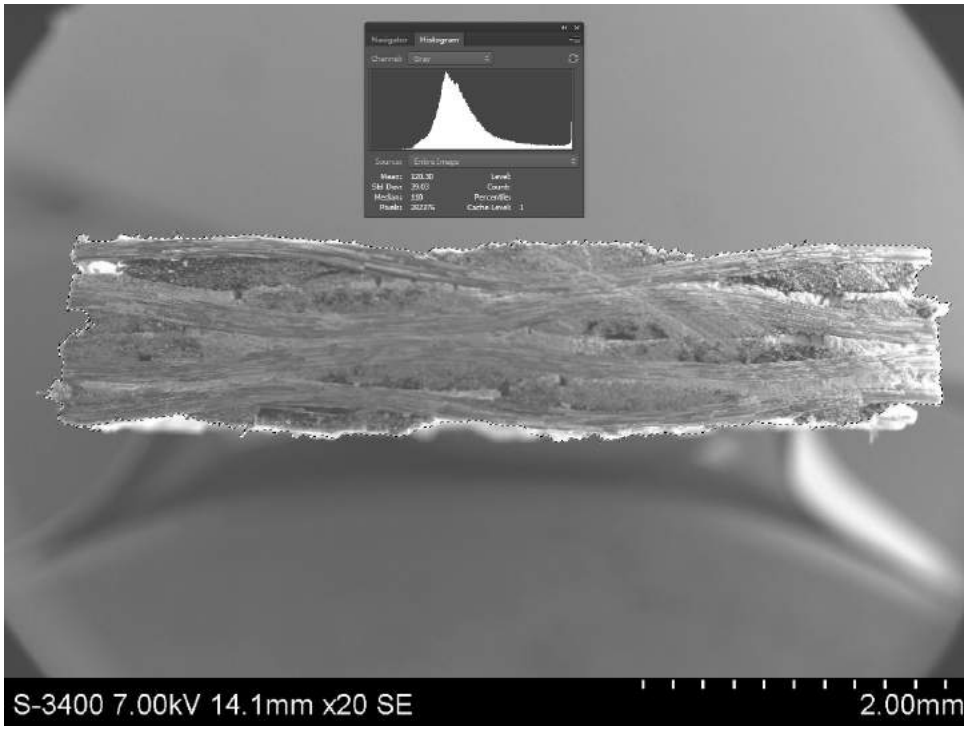

Figure 3.8. Cross section pixel counting.

Table 3.3. Pixel counts for all specimen cross sections.

	Area Pixel Count	Legend Scale (mm)	Legend Pixel Count	Area Ratio	Cross Section Area(mm^2)
R252-1	319729	5.87	1229	0.2117	7.29
R252-2	238377	6.04	1104	0.1956	7.14
R252-3	330617	5.81	1211	0.2254	7.61
R252-4	300896	6.16	1264	0.1883	7.15
R253-1	299918	5.94	1242	0.1944	6.86
R253-2	270473	5.82	1167	0.1986	6.50
R253-4	301574	5.98	1241	0.1958	7.00
R253-5	308825	5.94	1252	0.1970	6.95
R254-2	278740	5.67	1192	0.1962	6.31
R254-3	263451	5.52	1137	0.2038	6.21
R254-4	282376	5.54	1175	0.2045	6.28

The pixel counted cross section areas are compared to the calculated areas from micrometer measurement to explore the differences between the two measurement methods. When incorporated into the material property calculations, the adjusted area measurements directly influence ultimate stress data.

Table 3.4. Comparison of area measurement methods.

	Cross Section Area (mm^2)		
	Mean Area Method	Pixel Counting Method	% Difference
R252-1	7.25	7.29	(-0.564)
R252-2	7.75	7.14	7.99
R252-3	8.66	7.61	12.1
R252-4	7.67	7.15	6.85
R253-1	8.14	6.86	15.8
R253-2	7.27	6.5	10.6
R253-4	7.42	7.00	5.66
R253-5	7.55	6.95	7.89
R254-2	6.87	6.31	8.20
R254-3	6.95	6.21	10.7
R254-4	6.90	6.28	8.97

3.4 Adjusted Property Calculations

As the stress scales proportionally to the change in cross sectional area, the elastic modulus calculated for each tensile specimen also changes accordingly. Using this method, the mechanical property measurements for all samples vary significantly; both the tensile strength and elastic modulus calculations differ a maximum of approximately 14% in both cases (Table 3.5), which is clearly visible in Figure 3.9. For the most part, this alternative area calculation method increases the strength (Figure 3.10) and the stiffness (Figure 3.11) measurements of the test samples. An anvil

micrometer measurement assumes the cross-section of the material under test (MUT) is quadrilateral and fully dense. Since the CMC is not fully dense and has inherent voids, its cross-sectional area is smaller, which proportionally increases the calculated stress on the part. R252-1 in Table 3.4 is an exception, likely because the micrometer measurement was not taken at exactly the same location as the SEM photograph.

Table 3.5. Comparative statistics of measurement methods (in MPa).

	Elastic Modulus		Ultimate Tensile Str.		% Difference	
	Micrometer Measured	Analytically Measured	Micrometer Measured	Analytically Measured	Elastic Modulus	Tensile Strength
Mean	836.0	912.79	101.8	111.1	9.190	9.210
Std. Error	28.12	24.91	3.587	3.273	11.42	8.753
Median	860.7	926.7	103.1	114.3	7.672	10.80
Std. Dev.	93.27	82.62	11.90	10.86	11.42	8.753
Range	311.2	308.8	37.70	34.88	0.7584	7.486
Minimum	626.0	711.59	77.20	87.75	13.67	13.67
Maximum	937.2	1020	114.9	122.6	8.878	6.725

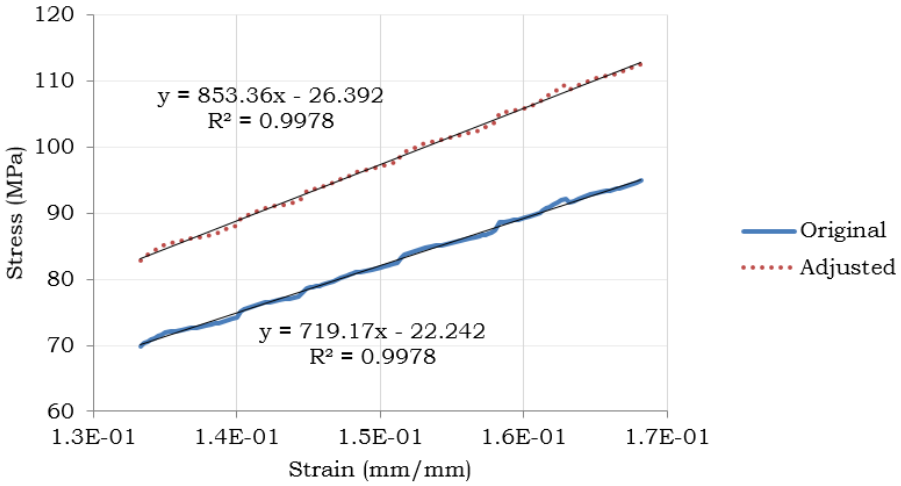

Figure 3.9. Stress-strain curves of R253-1 (or simply 3-1) for both area measurement methods.

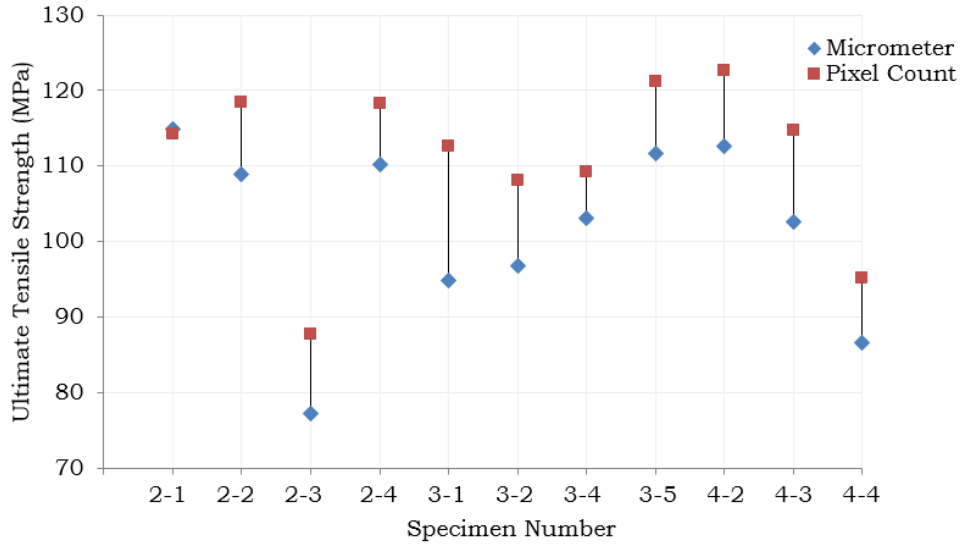

Figure 3.10. Specimen strength comparison of measurement methods.

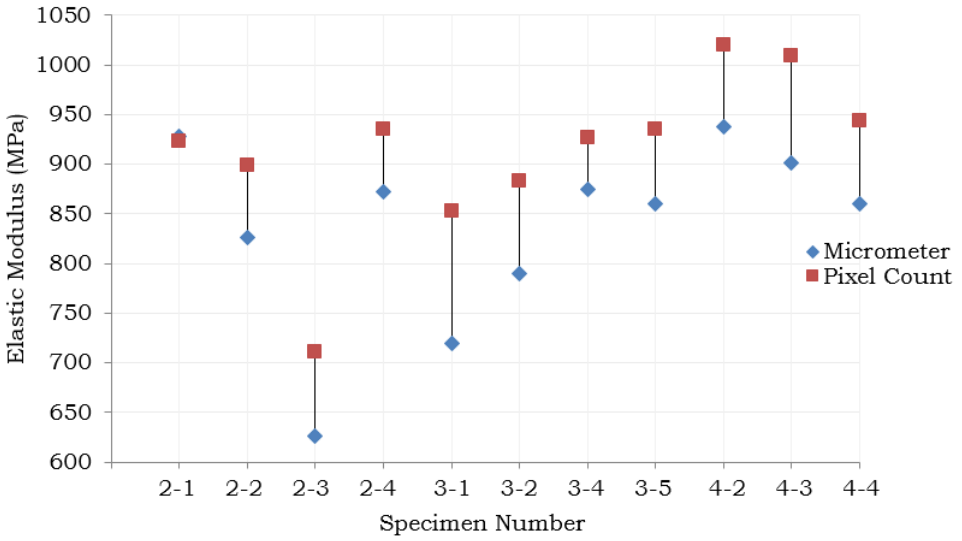

Figure 3.11. Elastic modulus comparison of measurement methods.

3.5 Statistical Analysis

Since composites are anisotropic, the variation between sample data can be significantly greater than isotropic, homogeneous materials. This means statistical data treatment is especially important in establishing composite mechanical properties. The Weibull statistic is often used for this purpose with polymer, metal, and ceramic composite strength data of varying sample sizes (Barbero, et. al., 1992). The probability of failure using a Weibull distribution is described by the function

$$F(\sigma) = 1 - exp\left[-\left(\frac{\sigma}{\sigma_0}\right)^m\right] \tag{3.5}$$

Where F is the failure probability of a sample under tensile stress σ, m is the shape parameter, and σ_0 is the scale parameter, similar to the mean material strength. The shape and scale parameters need to be determined, so eq.(3.5) is linearized with a double logarithm function and these factors are isolated.

$$ln\left[ln\left(\frac{1}{1-F(\sigma))}\right)\right] = m * ln\sigma - m * ln\sigma_0 \tag{3.6}$$

and $F(\sigma)$ is estimated with the equation

$$F_i = \frac{i - 0.5}{n} \tag{3.7}$$

where i is the sample number and n is the total number of samples, in this case, the 11 successful tensile tests. The resulting m and σ_0 parameters are then used in eq.(3.5) to build the 95% confidence level probabilistic failure model in Figure 3.12, which is used to determine strength values that correspond to 99% and 90% material

survivability estimates. These survivability rates are respectively known as the A-basis and B-basis material properties.

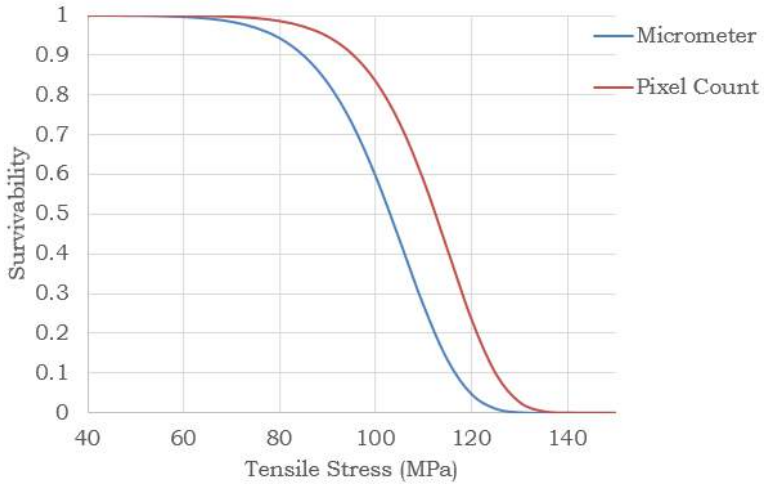

Figure 3.12. Weibull distribution of calculated tensile strength for the micrometer (blue) and pixel counting (red) cross-section measurement methods.

From this model, the A and B basis material properties are determined and tabulated in Table 3.6 for both the micrometer and the analytical area measurements. These are the material strength values that can be used for component design, and the arithmetic mean can be reported as the officially measured maximum (ASTM, 2014).

Table 3.6. A-basis and B-basis tensile strength data.

	Ultimate Tensile Strength (MPa)		
	A-Basis (99%)	B-Basis (90)%	Mean
Micrometer Measured	66.66	84.89	101.8
Analytically Measured	77.54	95.37	111.1

4. Failure Analysis

The fractured C/SiC CMC samples are investigated to test the failure hypothesis: since the system is uncoated, brittle matrix-dominated fracture is expected, and the amount of fiber pullout on the fracture surface should be minimal. Data was gathered through experimental observation and post-fracture microscopy using a Hitachi S-3400 variable pressure scanning electron microscope (VP-SEM).

4.1 Microstructure Analysis

Based on the stress state of the material imposed by the testing machine, ceramic tensile failure and crack propagation are the considered failure modes. Therefore, both matrix and fiber were scrutinized for inter and intragranular crack formation. Since the CMC was produced using the PIP process, this investigation also serves to verify the polymer has fully converted into a ceramic. In Figure 4.1 (page 43), the macroscopic roughness in most of the matrix indicates intergranular crack formation similar to the area encircled and labeled. Intragranular cracks are more sparse and appeared as smooth areas of matrix material, but the presence of both validates the inspection paradigm.

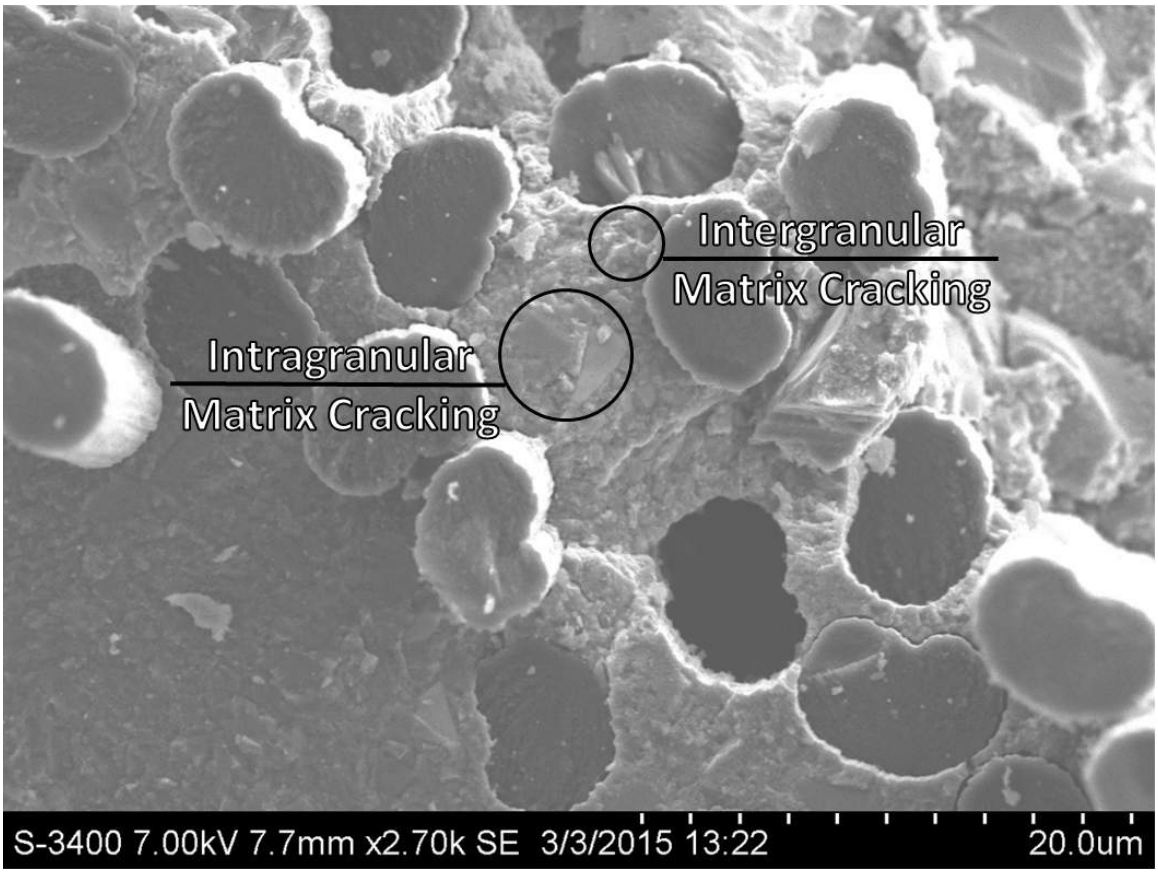

Figure 4.1. R253-1 fracture surface.

Tensile failure of carbon fiber was expected to be brittle, exhibiting similar fracture characteristics to the SiC matrix. Fiber pullout was minimal (Figure 4.2), and in some cases non-existent where fiber and matrix fracture surfaces are flush with one another, but it is much more prominent than it is in the uncoated SiC/SiC CMC photographed in Figure 1.12. This is reasonable, since carbon and silicon carbide's dissimilarities can allow for some fiber slipping, but nowhere near as much as the coated CMC system seen in Figure 1.11.

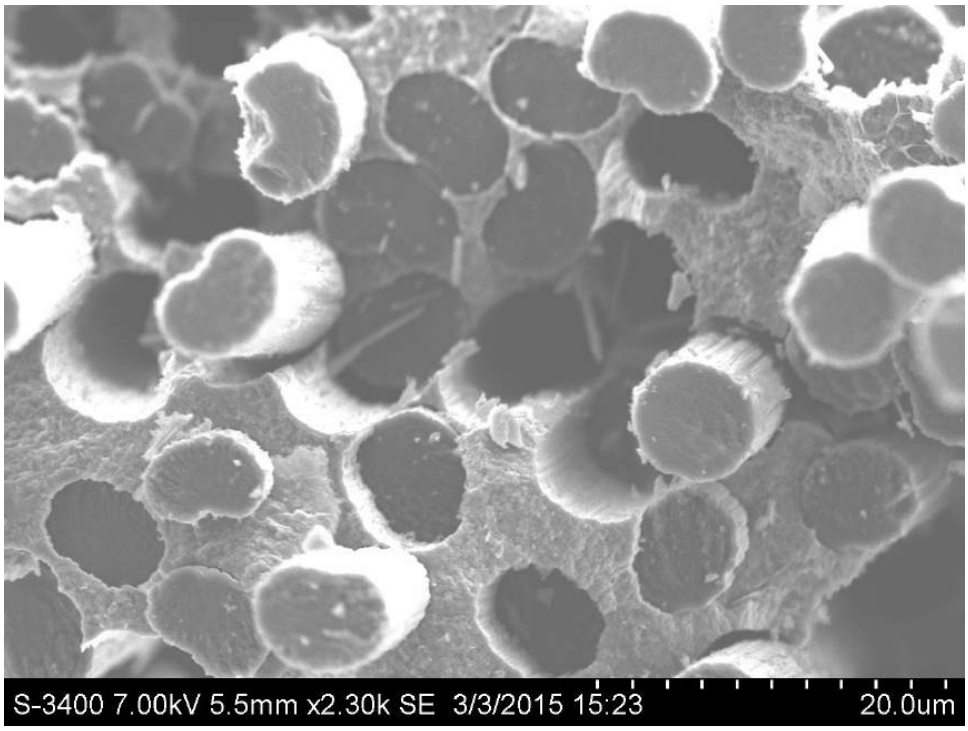

Figure 4.2. Fiber pullout in sample R252-4.

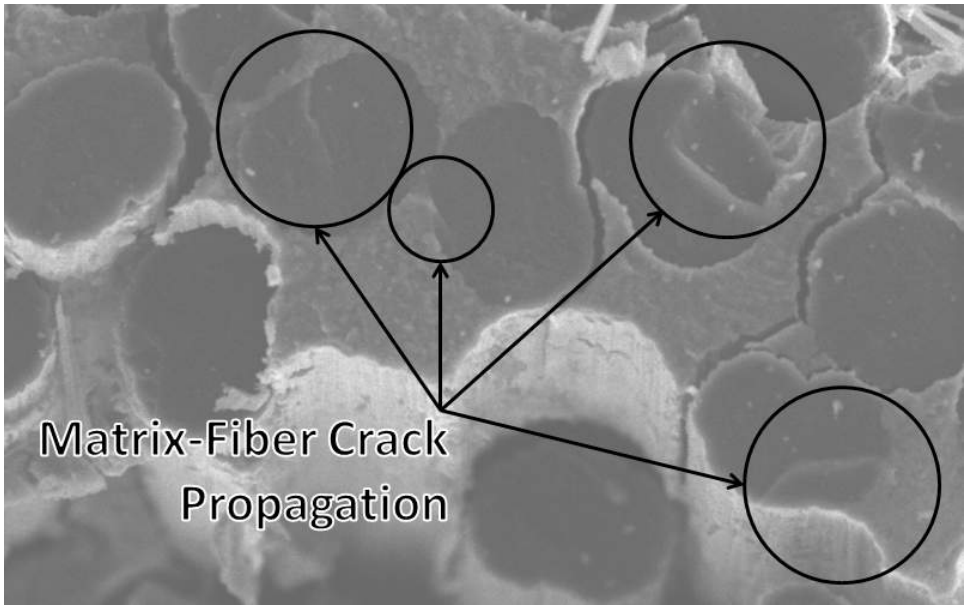

Figure 4.3. R252-3 fracture surface.

Some fibers fail individually because they separate from local matrix cracks, and at times could be heard during tensile testing as small twangs distinct from total sample fracture.

These sounds were minimal, and the more dominant crack growth mechanisms are clearly identified in the encircled areas in Figure 4.3, showing continuous crack growth from matrix to fiber. These cases exemplify matrix-dominated fracture from stress concentrations related to high interfacial bonding between the constituents. The nature of the spontaneous, catastrophic sample fracture transverse to the tensile force experienced in testing indicates the dominance of matrix crack propagation over cumulative fiber damage as the failure mode.

5. Discussion, Conclusions, and Recommendations

5.1 Discussion

Initially, the greatest concern was having enough samples to test to achieve the 5 successful test minimum recommended by ASTM standard C1275. With 11 successful tests, this proved not to be as much of a challenge as foreseen. If testing material supply were not a concern, wider tensile specimens could have been prepared which would have reduced the preform's contribution to property variation, as some specimens had more longitudinal tow volume than others. Small sample size proved to be a degrading factor for other reasons as well. The small gage width made it difficult to install strain gages on the dummy specimens for test alignment, resulting in the destruction of numerous strain gages due to mishandling. As a result, there was not sufficient time to procure equipment for a redundant specimen to use upon the failure of the first gaged specimen in order to complete the 5 alignment runs required by test protocol E1012. Ultimately, ASTM C1275's recommendation that the load train be verified at least once before beginning a series of tests was indeed satisfied.

Of the 14 CMC specimens tested, 3 failed at locations in the immediate vicinity of the compression fixtures. C1275 recommends a load rate that causes fracture within 10 seconds to "minimize environmental effects when testing in ambient air" (ASTM, 2014), but actual time to fracture ranged between 17 and 21 seconds. Since

the load rate was still quasi-static and the laboratory environment was not hostile, this discrepancy was not considered significant enough to alter the load rate and add unnecessary variants to the testing procedure

Examination of the specimens cross sections revealed that their geometry was irregular and not the simple rectangle that would be expected from micrometer measurements. The deviations from that ideal shape induce significant error in the determination of stresses. Directly measuring the failure cross sectional area under the microscope after each test allowed the production of more accurate stress results.

Such a measurement is possible because no necking occurs given that the fracture is brittle. However, percent strain at fracture measurements for some samples reached nearly 18%, which is inconsistent with the brittle assumption and would imply that the CMC is more ductile than expected (the S400 reference CMC failure strain is 0.53%). The lengthening of crimped fibers can be a contributing factor to a high strain percentage at failure, particularly with uncoated fibers, but not to such an extent as almost 2 orders of magnitude above the strain data for T300 carbon fiber or the S400 reference CMC. Another contributor to this data discrepancy was the compliance of the epoxy used to glue the tabs to the specimen, but it is highly likely that the greatest source of error resulted from using load train displacement data instead of strain gage or extensometer measurements. This contradiction between material stiffness and strain at failure is evidence that the strain measurements are inaccurate and, therefore, will not be used.

The failure modes from microscopic analysis were consistent with expectations. However, the limited magnification power of the aged SEM used barred one important feature from being inspected clearly - the fiber fracture surface. While it is abundantly clear that the carbon fiber reinforcements failed in tension, they would have provided a continuous, unobstructed surface upon which to examine fracture feature lines from crack propagation. Without this data, the assumption of tensile fiber failure cannot be explored further using microstructural evidence.

In Table 5.1, the reference CMC data from page 22 compared to the gathered CMC performance data reveals significant similarities and differences.

Table 5.1. Mechanical property comparison with S400 reference CMC (in MPa).

	Tensile Strength	Yield Stress	Young's Modulus	Strain at Failure
Micrometer Meas.	101.8	-	835.9	15.8%
Analytically Meas.	111.1	-	912.8	15.8%
S400 Ref. CMC	289.6	98.6	109.6	0.53%

First, the ultimate tensile strength of the C/SiC is closer to the yield strength of S400 C/SiC instead of its tensile strength. Most likely, this is due to the S400's interfacial coating and heat treatment, responsible for a higher damage tolerance.

Fiber strength is the primary factor in composite tensile strength. Therefore, any source of fiber degradation will reduce the CMC strength properties far more than any other adverse effects. While each of these two composites may differ in many more ways, their similarities provide a reasonable validation for the success of the tensile test and its ability to measure material strength.

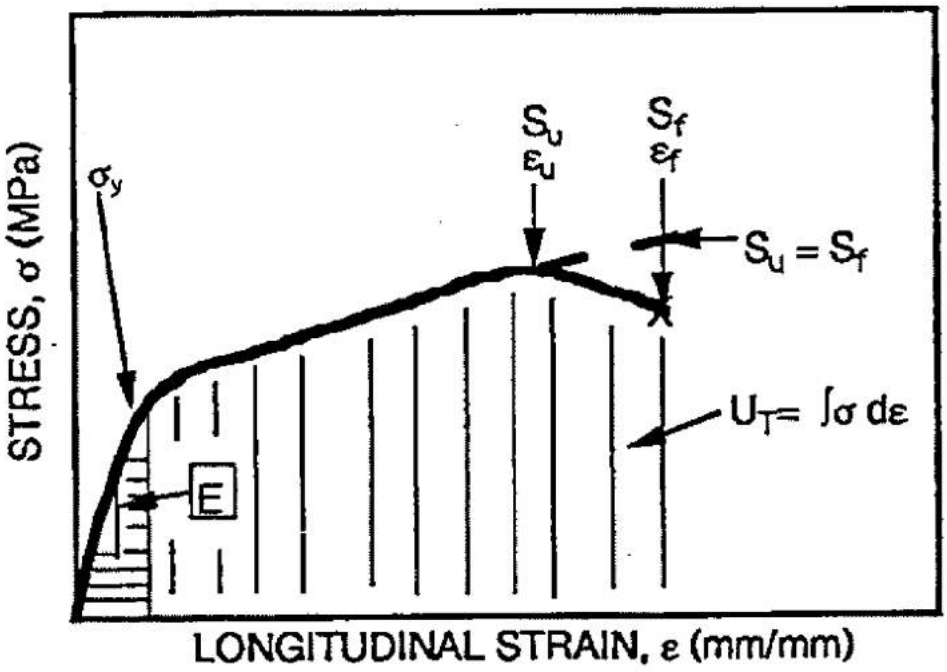

Figure 5.1. Failure of a damage tolerant CMC with existent yield stress (ASTM, 2014).

The strain at failure and elastic modulus, as previously mentioned, differ substantially. The potential error sources contributing to poor strain measurements in turn propagate to elastic modulus calculations despite confidence in stress measurements. While the tensile testing procedure is sound for ultimate stress analysis, measurement of strain should be improved before strain and elasticity can be determined with similar confidence using this test method. The data regarding strain and elastic modulus in their current state are not reliable.

Analysis of material failure revealed results within expectations. The fracture of uncoated fibers, both flush with the matrix and with some fiber pullout, indicate

tensile failure, and the topography of the matrix cracks closely correlates with neighboring fiber cracks, verifying a substantial amount of interfacial bonding between the two constituents. The "ungraceful" fracture and its surface topography seem to corroborate this hypothesis, as a coated fiber system would exhibit cumulative fracture, showing substantially more fiber pullout.

5.2 Conclusions

Monotonic, uniaxial tensile testing was effective at measuring the tensile strength of the CMC material and consistent with data from a similar, independent material.

Load train displacement was an ineffective method for calculating material strain, likely resulting in unreliable measurements for elastic modulus and strain-at-failure.

Analysis of fracture modes and material failure surfaces verified that CMC samples failed in tension with qualitatively minimal fiber pullout. Microstructural data suggests a strong correlation between lack of fiber coating and catastrophic material failure.

5.3 Recommendations

The largest contributor to improving strain data would be an extensometer, and all future tests performed should include one. One of the limiting factors in obtaining one for this study was specimen size, which should be increased not only to accommodate larger extensometers and decrease cost, but also to minimize variation

between specimens resulting from different longitudinal fiber volumes. This could be achieved either through preparing wider samples for an averaging effect, or through more precise machining of thin samples to control fiber direction and tow content.

Material strength can be improved by reducing fiber degradation during PIP processing. Epoxy deposits are present on all commercial grade carbon fiber and are a significant source of fiber degradation, therefore future CMC samples should have pretreated fibers to eliminate this issue. Additionally, fiber coating systems should be included in future tests so that coated and uncoated fibers and their failure modes can be investigated and compared.

The magnification power of the SEM used was limited. With a more powerful system, more complete microstructural data could be acquired to substantiate failure theories. Furthermore, interfacial fiber coating would be the smallest element in a CMC with respect to cross-sectional area, and further analysis of that constituent would benefit from improved magnification power.

REFERENCES

Ashbee, K. (1993). *Fundamental principles of fiber reinforced composites.* 851 New Holland Ave. Box 3535 Lancaster, Pennsylvania 17604: Technomic Publishing Company, Inc.

ASTM. (2014). Standard test method for monotonic tensile behavior of continuous fiber-reinforced advanced ceramics with solid rectangular cross-section test specimens at ambient temperature [Computer software manual].

Becker, W. T., & Shipley, R. J. (2002). *Asm handbook volume 11: Failure analysis and prevention.* Materials Park, Ohio: The Materials Information Society.

Bressers, J. (Ed.). (1995). A code of practice for the measurement of misalignment induced bending in uniaxially loaded tension-compression test pieces [Computer software manual]. Petten Site, Netherlands: European Commision: Institute of Advanced Materials.

Chawla, K. K. (2003). *Ceramic matrix composites.* University of Alabama at Birmingham: Kluwer Academic Publishers.

COI Ceramics, I. (2015). S400 typical properties [Computer software manual]. http://www.coiceramics.com/pdfs/6%20S400%20properties.pdf. ATK Aerospace.

Company, M.-C. S. (2015). *Machinable architectural 385 brass.* http://www.mcmaster.com/#9122k21/=12cryag.

Flexural strength tests of ceramics. (2012).

Krenkel, W. (2008). *Ceramic matrix composites: Fiber reinforced ceramics and their applications.* German National Library: Wiley-VCH.

Ogihara, S., Imafuku, Y., Yamamoto, R., & Kogo, Y. (2009). *Direct evaluation of fracture toughness in a carbon fiber.* http://www.iccm-central.org/Proceedings/ICCM17proceedings/Themes/Materials/HIGH%20PERFORMANCE%20FIBRES/D6.7%20Ogihara.pdf.

Steif, P. S., & Trojnacki, A. (1992). Bend strength versus tensile strength of fiber-reinforced ceramics.

Stig, F. (2009). *An introduction to the mechanics of 3d-woven fibre reinforced composites* (Unpublished doctoral dissertation). KTH School of Engineering Sciences, Stockholm, Sweden.

Toray. (2015). *T300 data sheet.* http://www.toraycfa.com/pdfs/T300DataSheet.pdf.

Tripp, D. E., Hemann, J. H., & Gyekenyesi, J. P. (1989). *A review of failure models for unidirectional ceramic matrix composites under monotonic loads* [Memorandum]. http://ntrs.nasa.gov/archive/nasa/casi.ntrs.nasa.gov/19890005099.pdf.

A. Appendix: Load vs. Displacement of Tensile Specimens

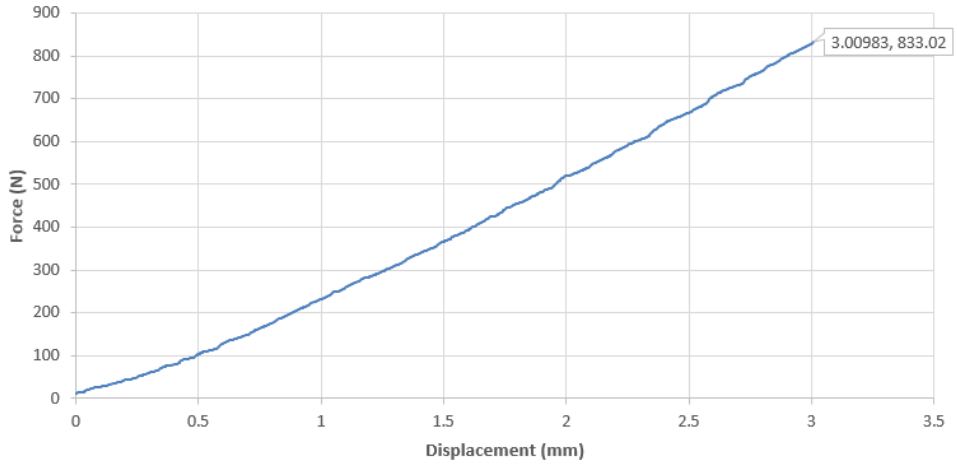

Figure A.1. R252-1 load vs. displacement.

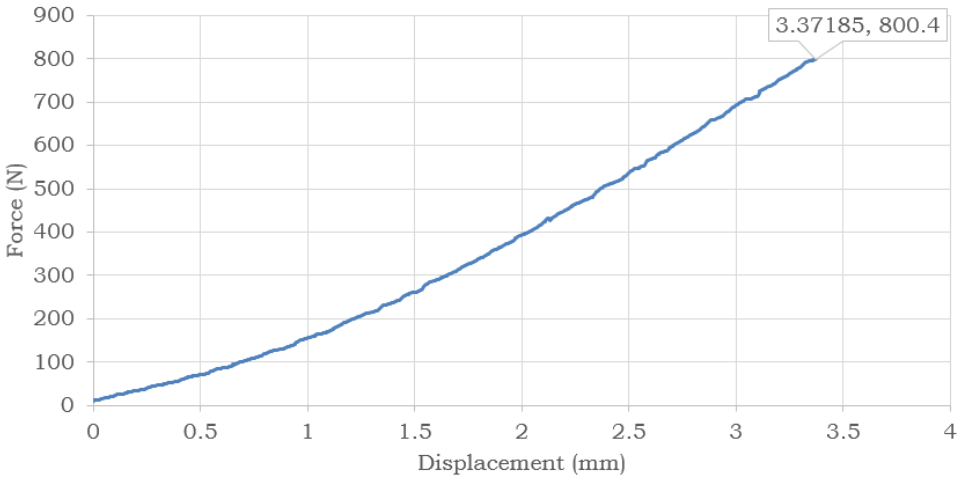

Figure A.2. R252-2 load vs. displacement.

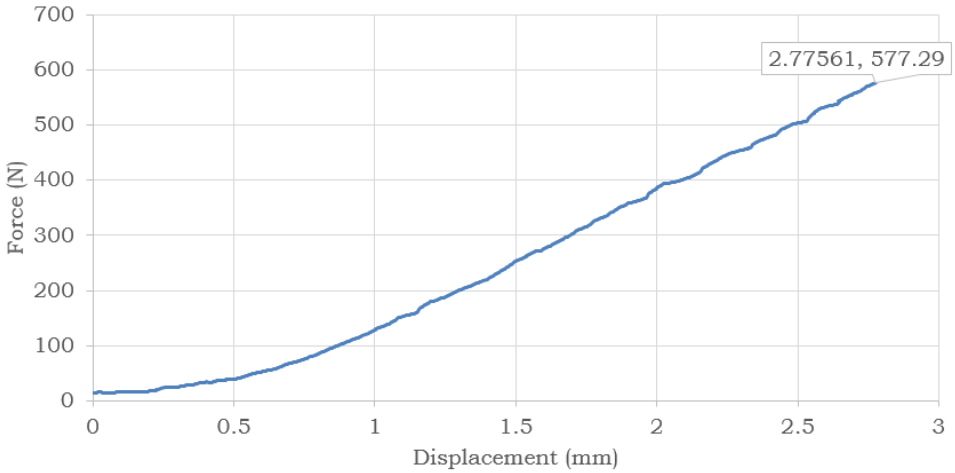

Figure A.3. R252-3 load vs. displacement.

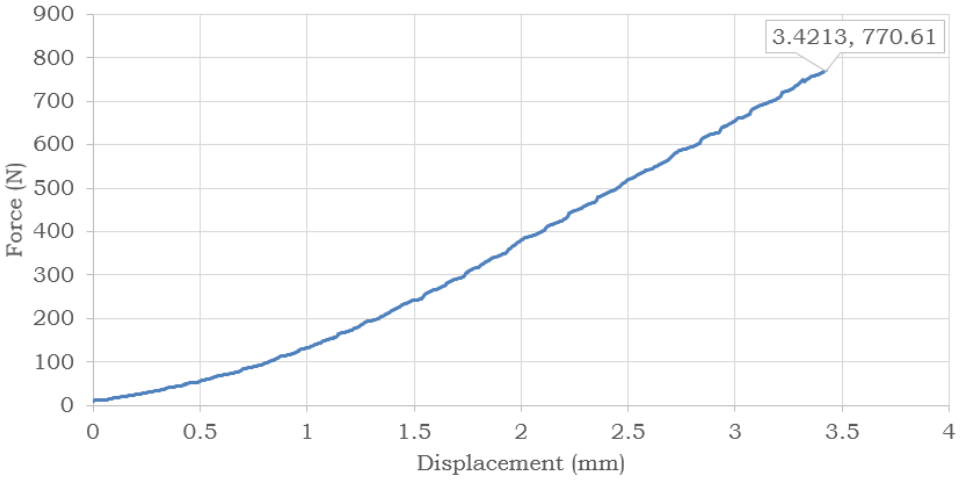

Figure A.4. R253-1 load vs. displacement.

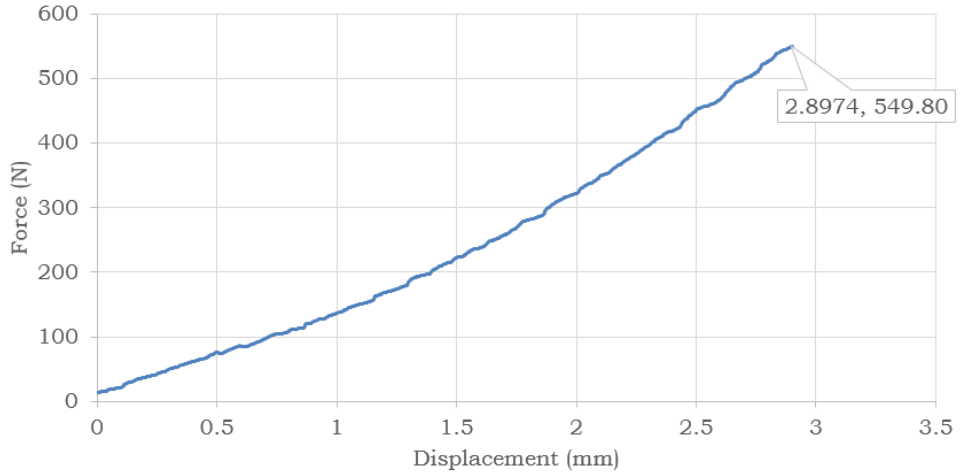

Figure A.5. R253-2 load vs. displacement.

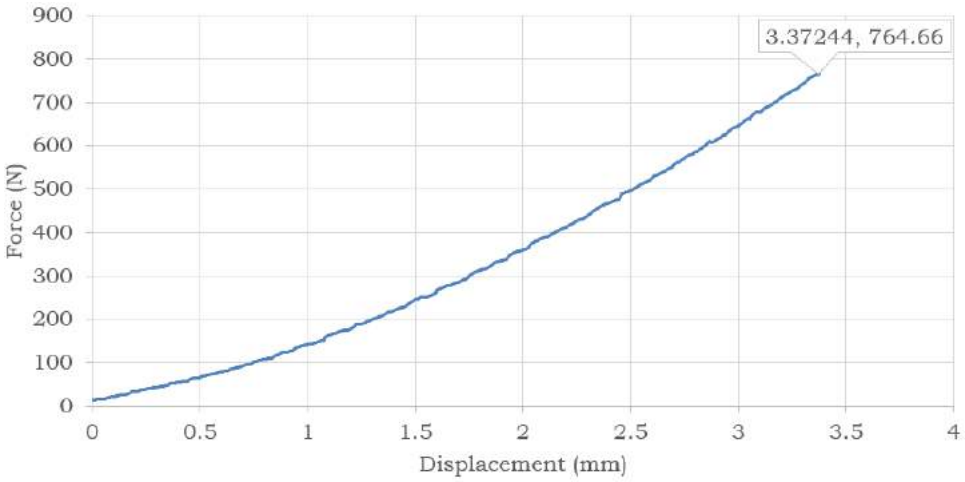

Figure A.6. R253-4 load vs. displacement.

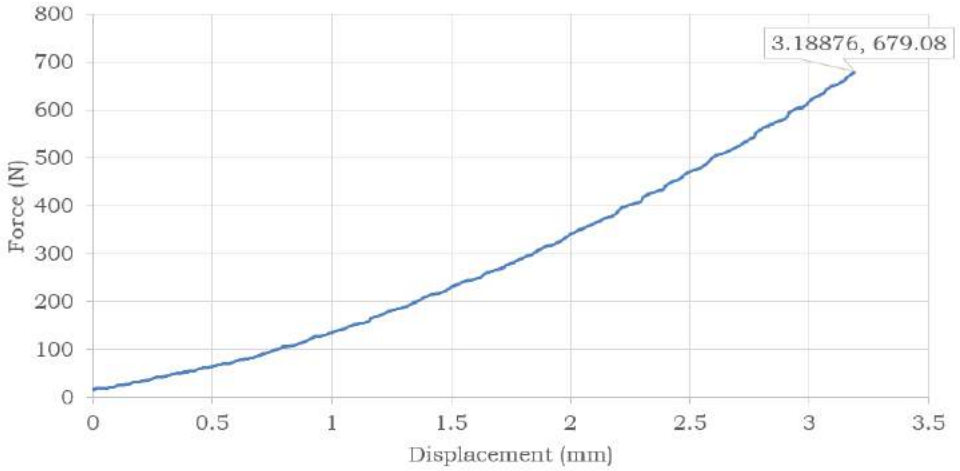

Figure A.7. R253-5 load vs. displacement.

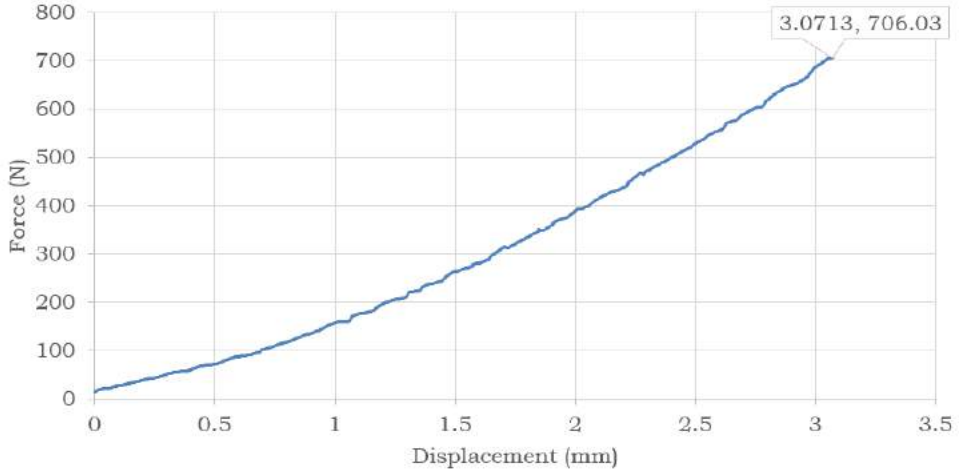

Figure A.8. R254-2 load vs. displacement.

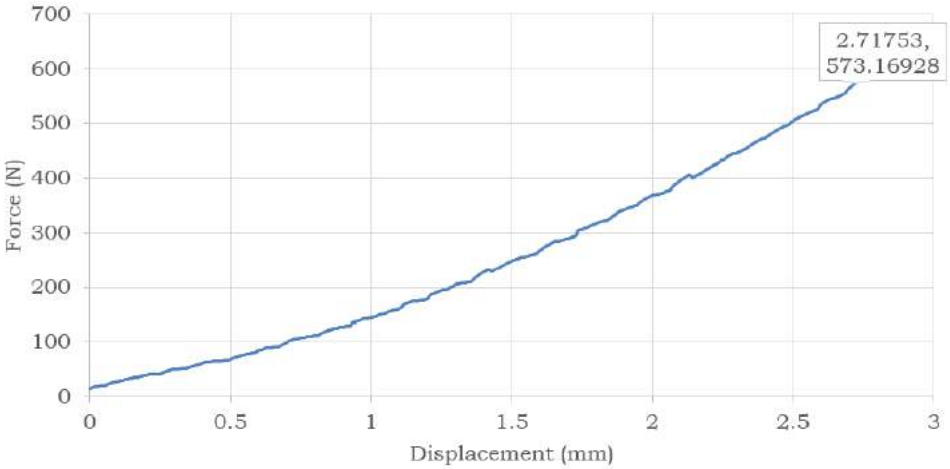

Figure A.9. R254-3 load vs. displacement.

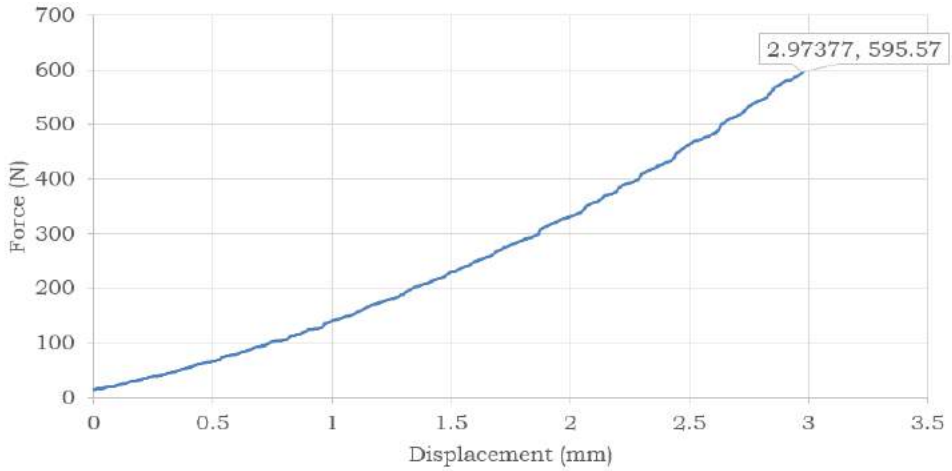

Figure A.10. R254-4 load vs. displacement.

B. Appendix: Fracture Surfaces of Tensile Specimens

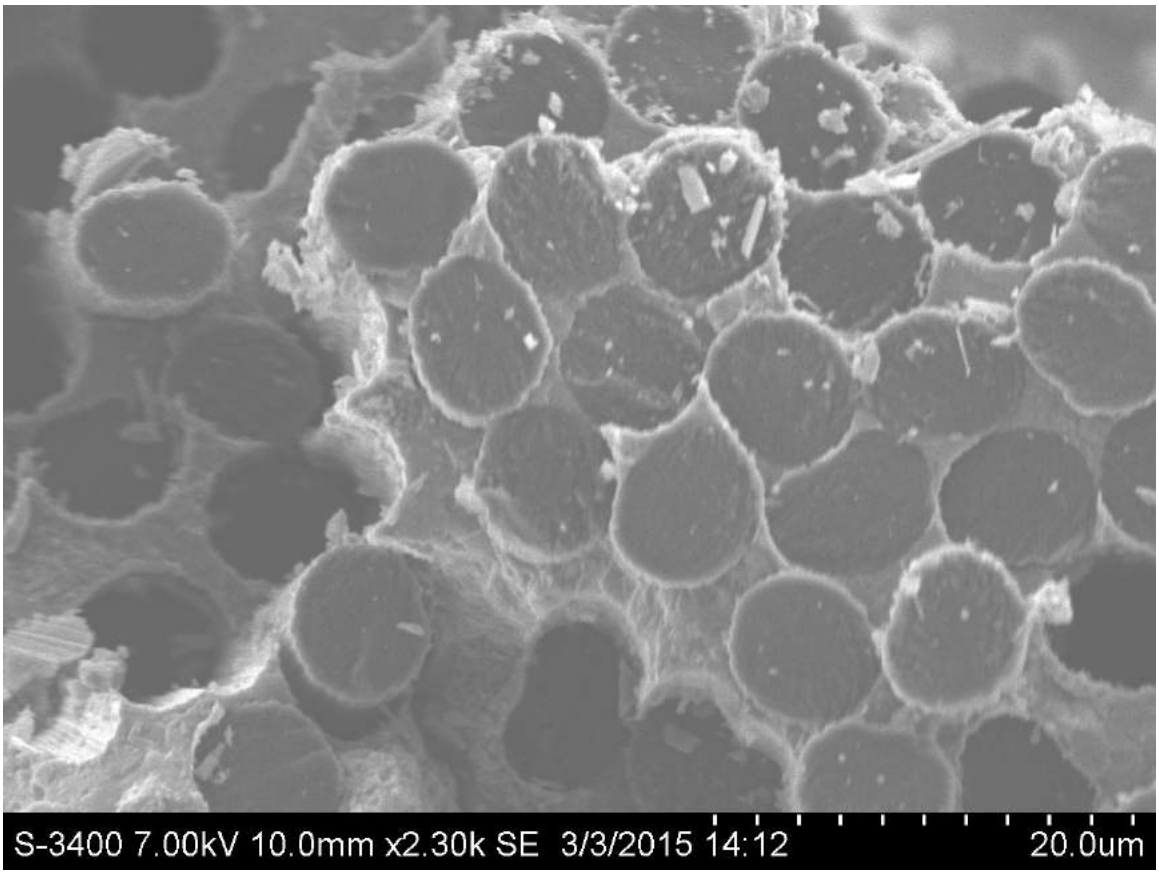

Figure B.1. R252-1 fracture surface.

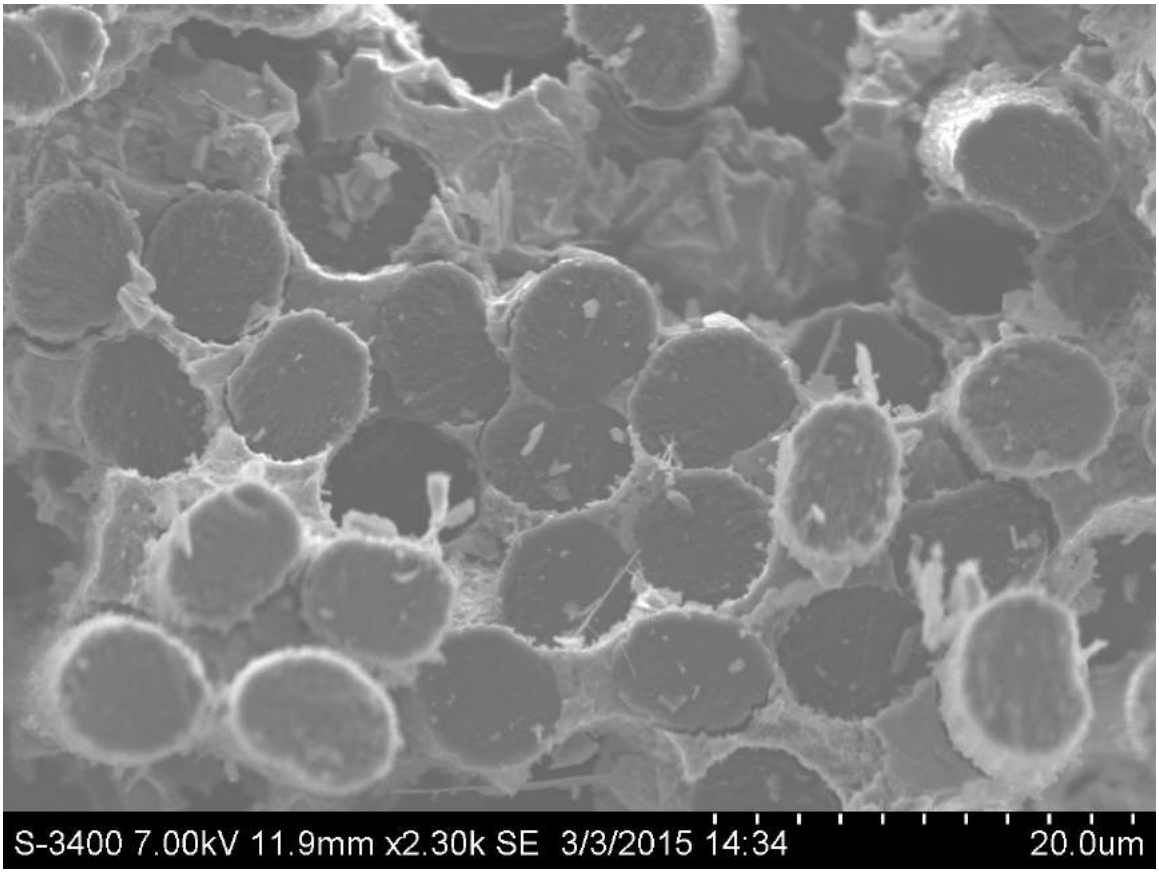

Figure B.2. R252-2 fracture surface.

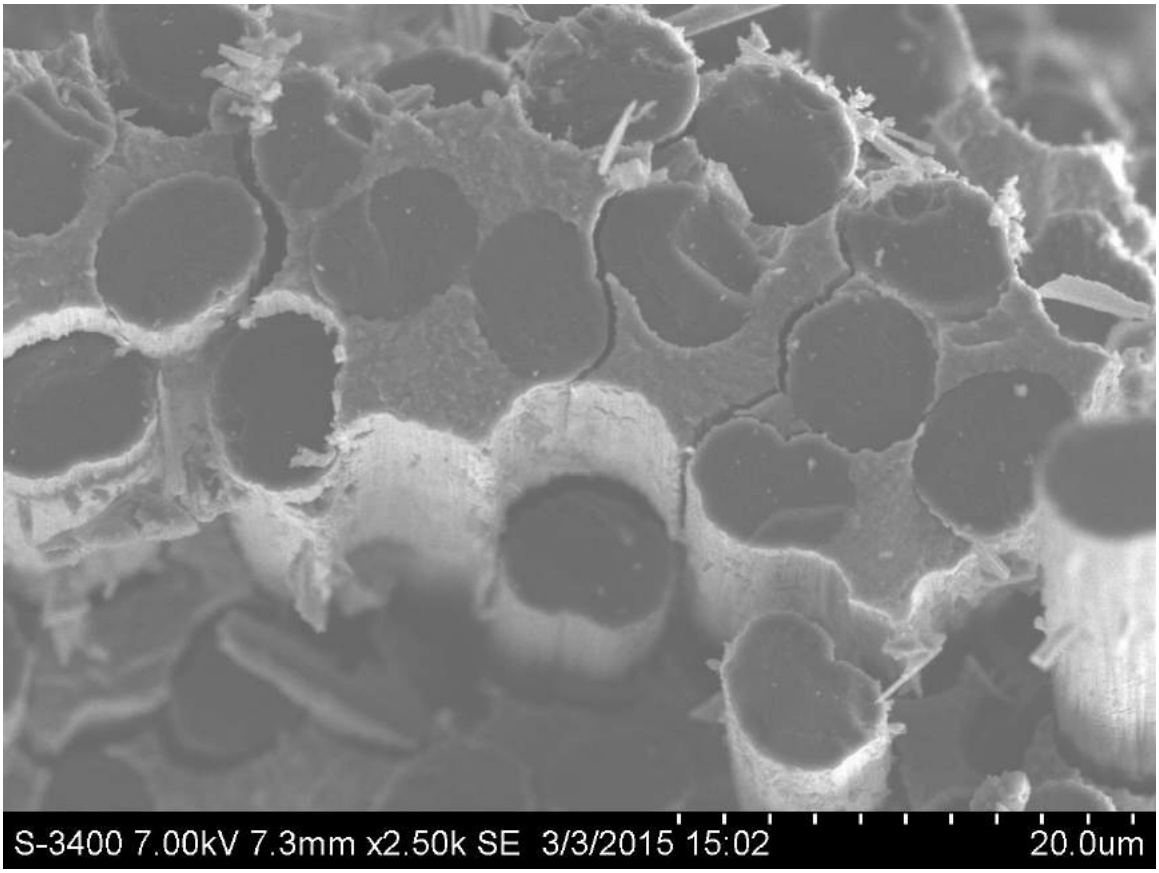

Figure B.3. R252-3 fracture surface.

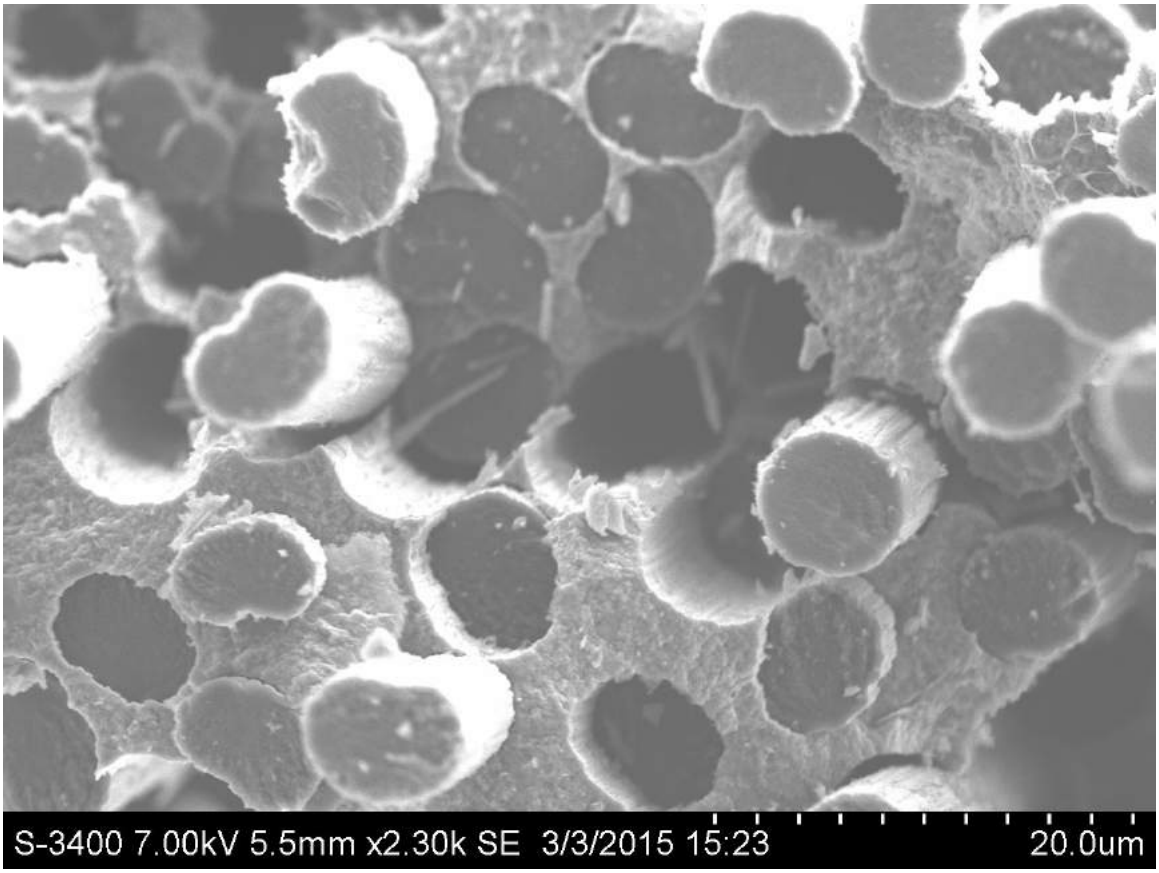

Figure B.4. R252-4 fracture surface.

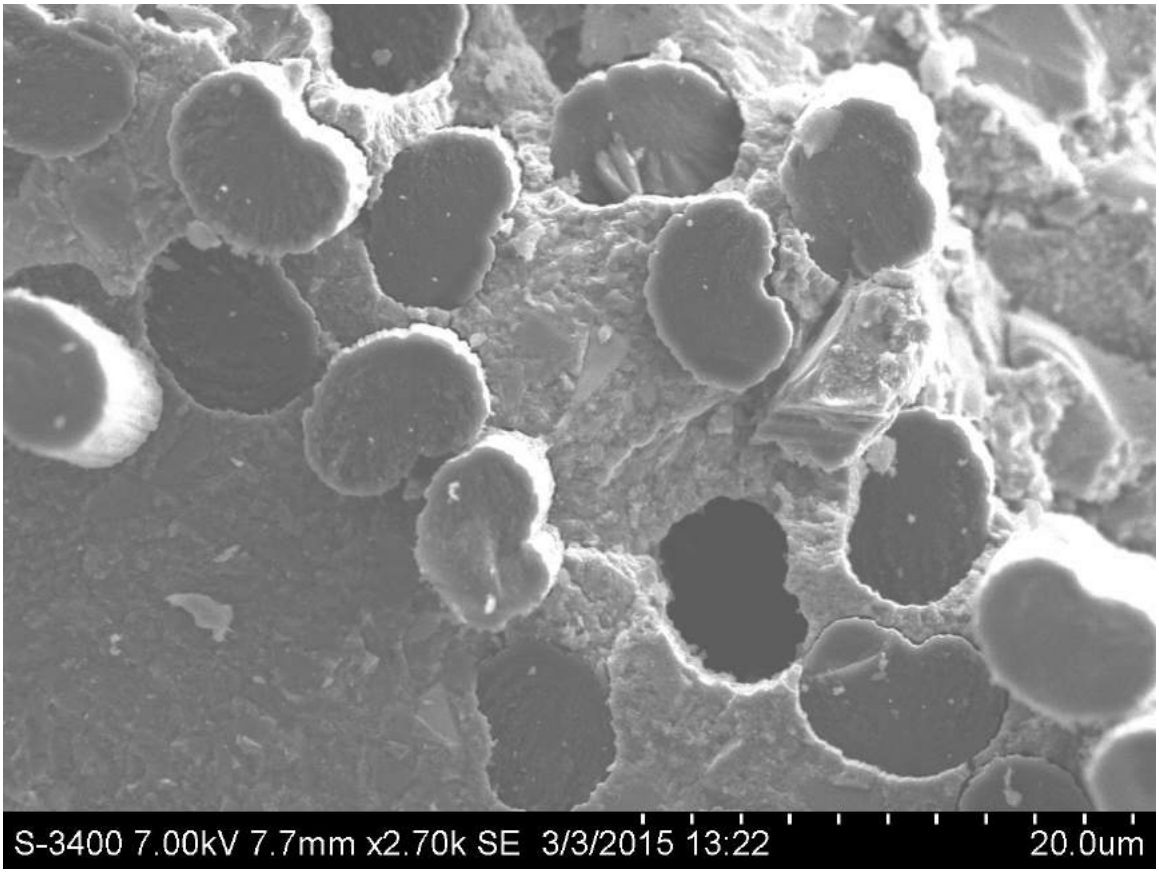

Figure B.5. R253-1 fracture surface.

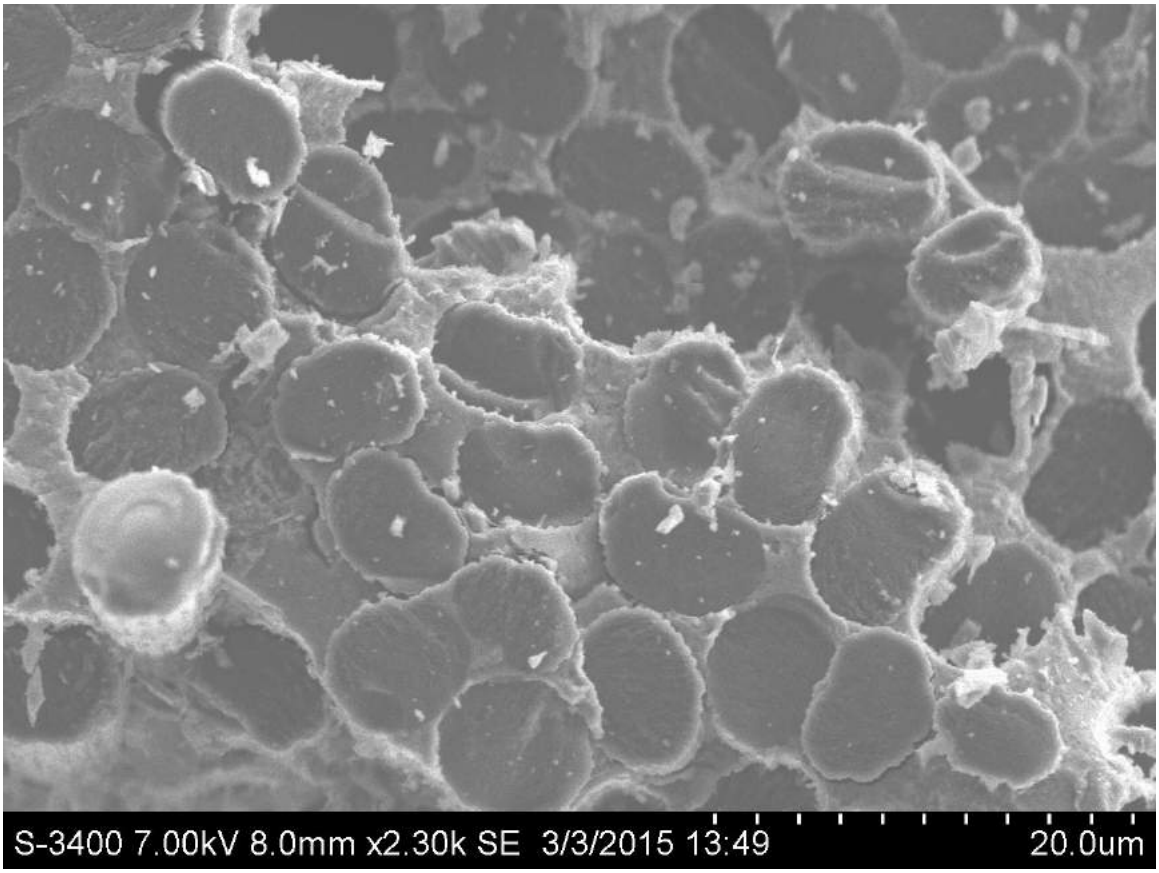

Figure B.6. R253-2 fracture surface.

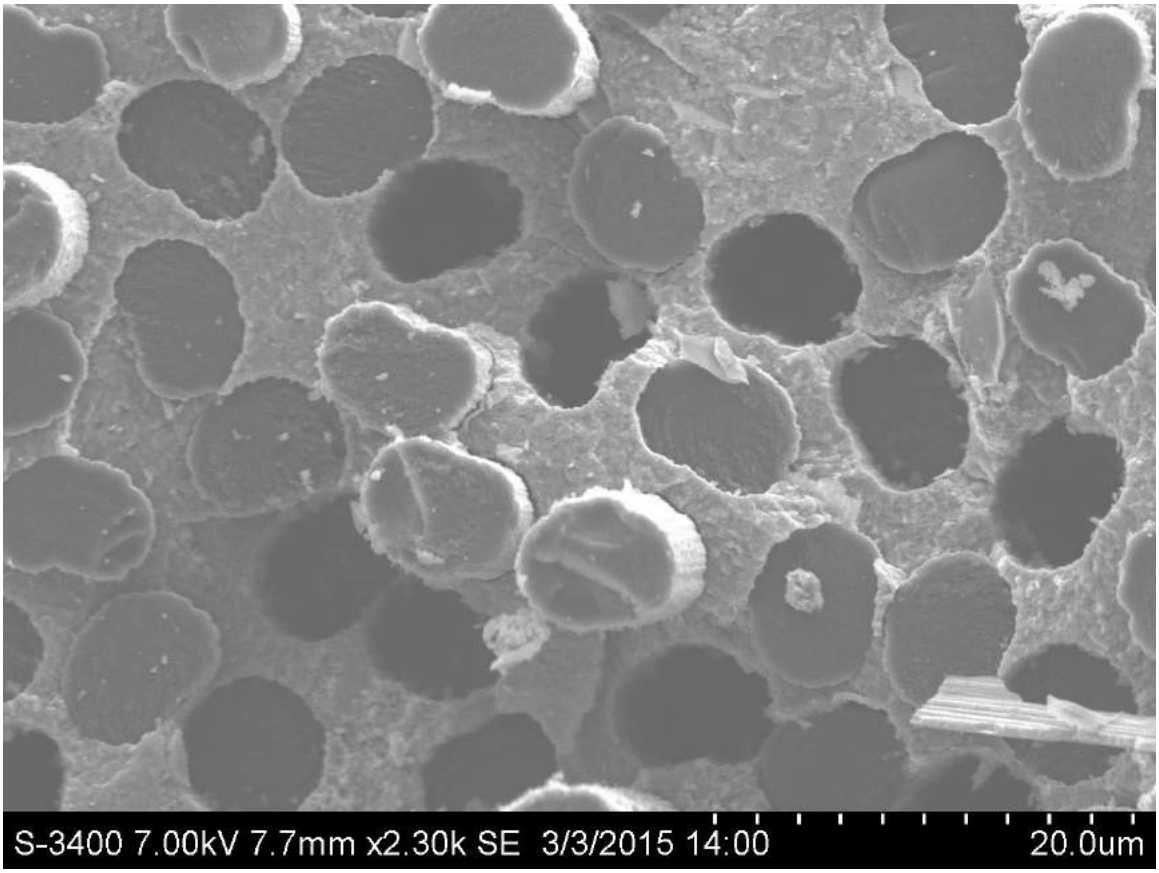

Figure B.7. R253-4 fracture surface.

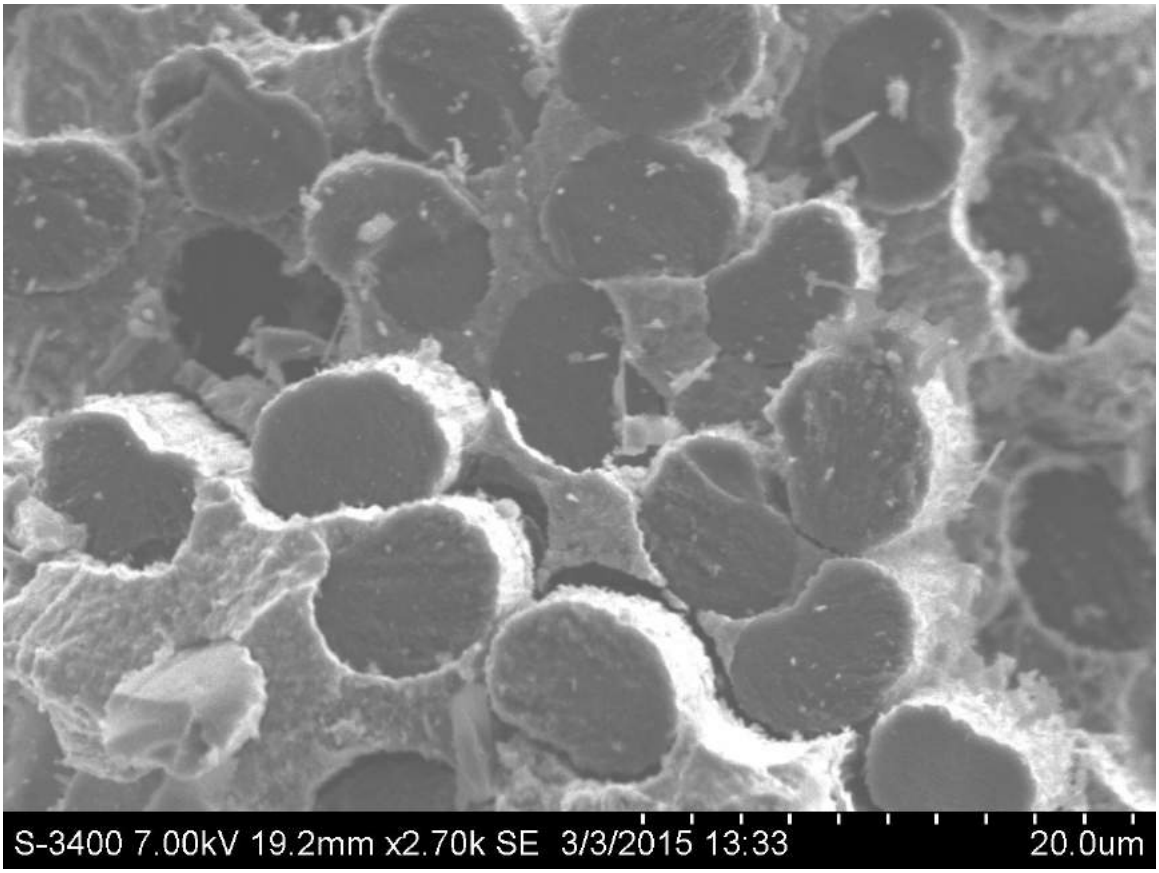

Figure B.8. R253-5 fracture surface.

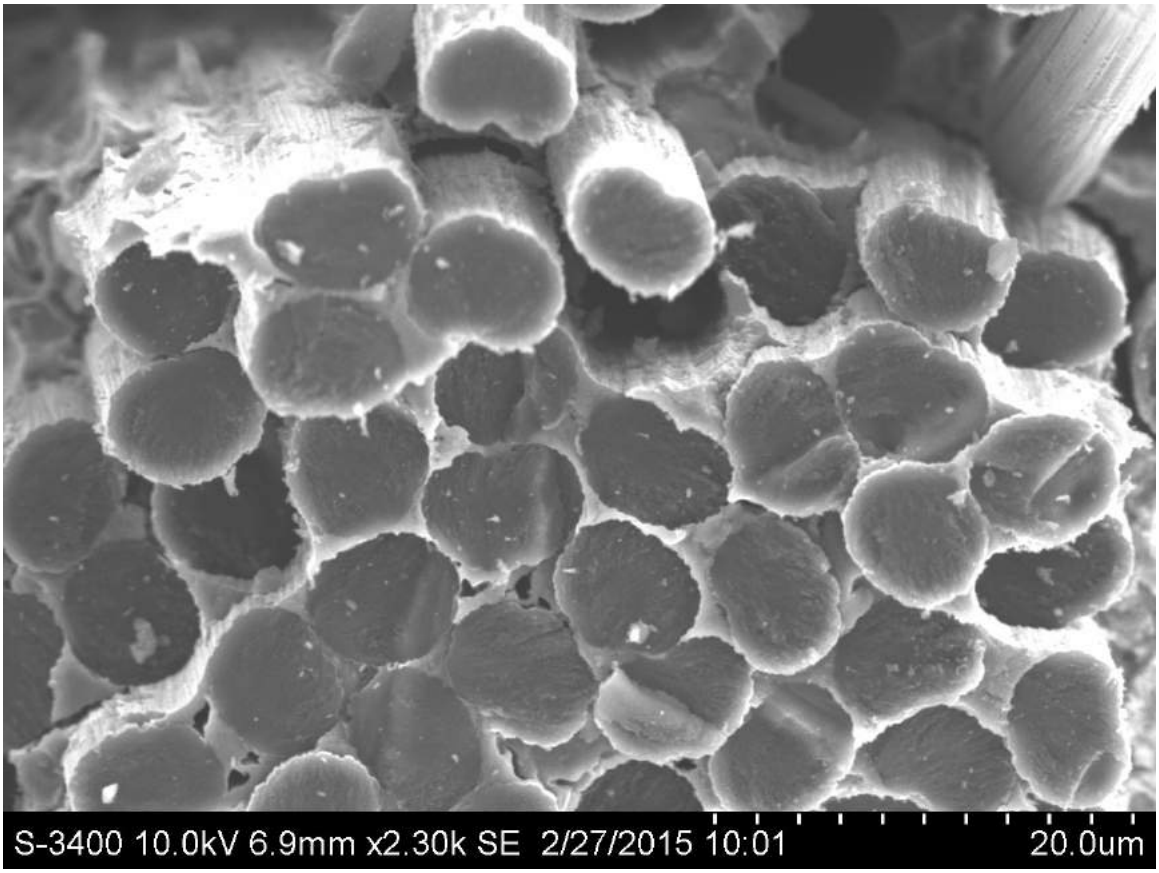

Figure B.9. R254-2 fracture surface.

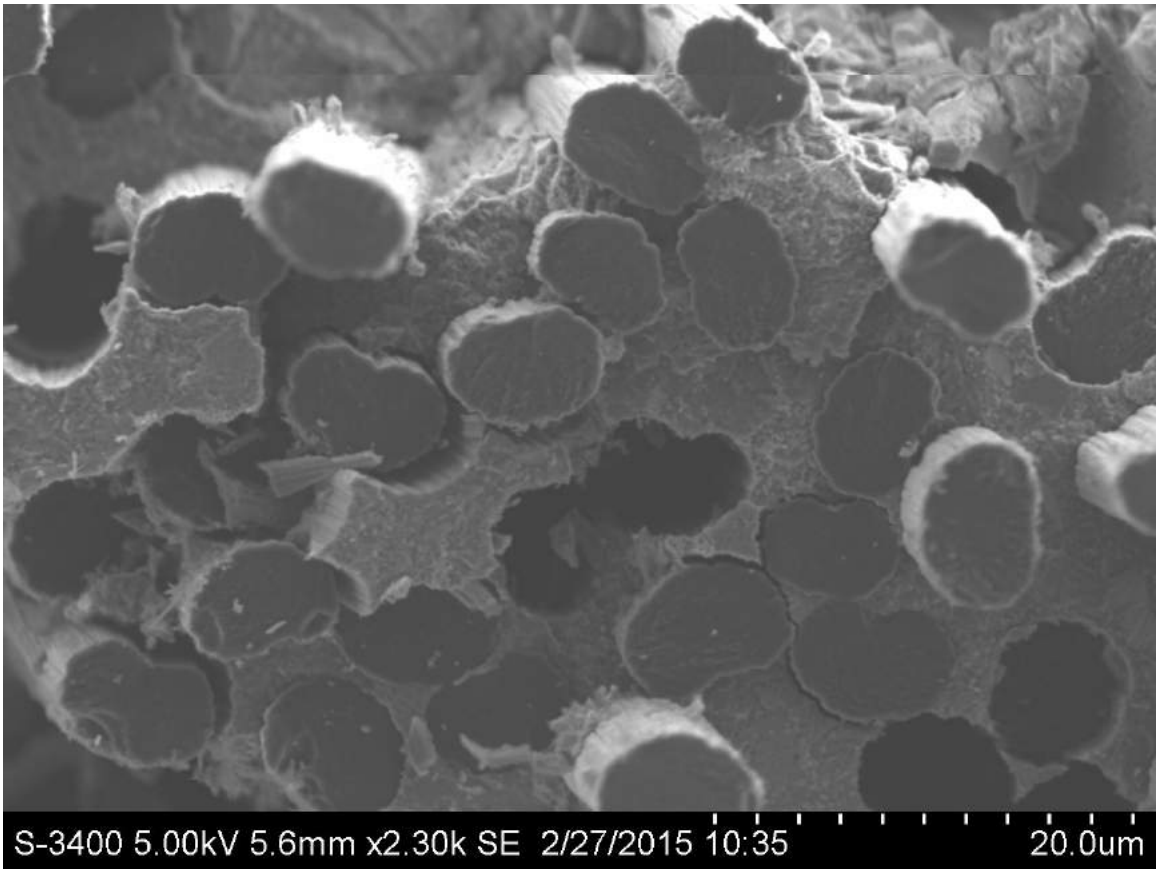

Figure B.10. R254-3 fracture surface.

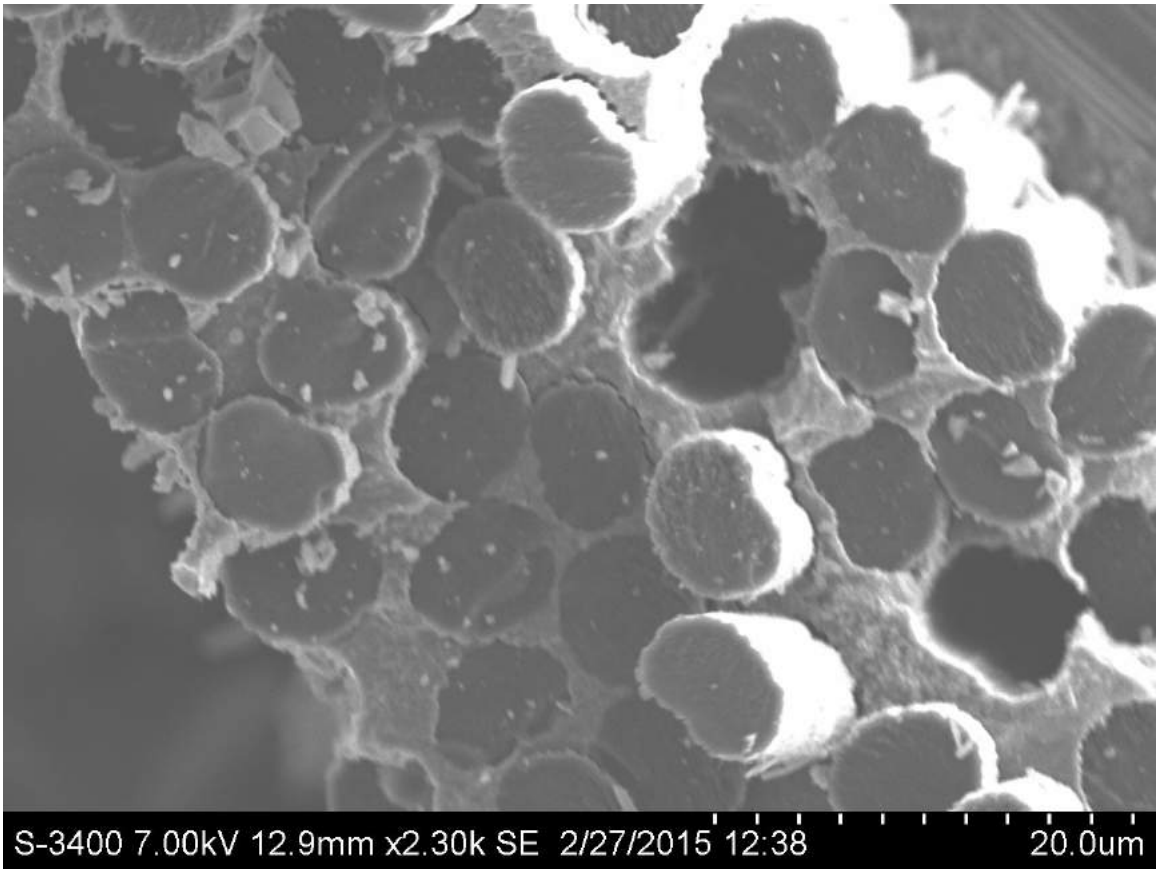

Figure B.11. R254-4 fracture surface.

C. Appendix: Statistical Regression of Strength Data

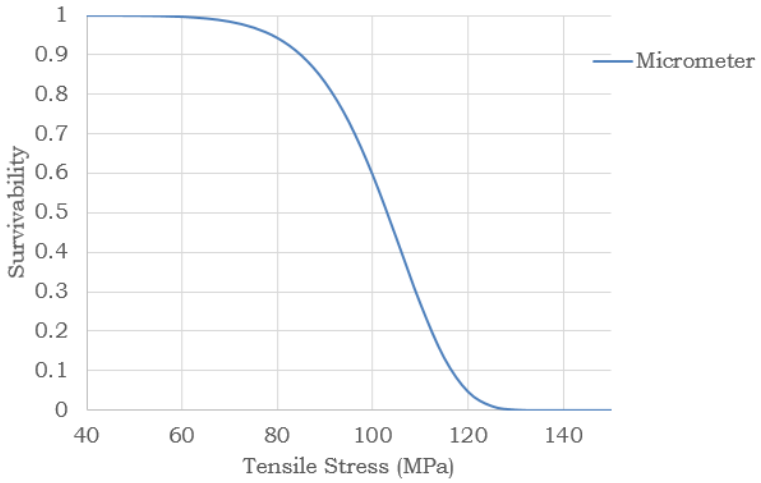

Figure C.1. Weibull survivability chart - micrometer measured.

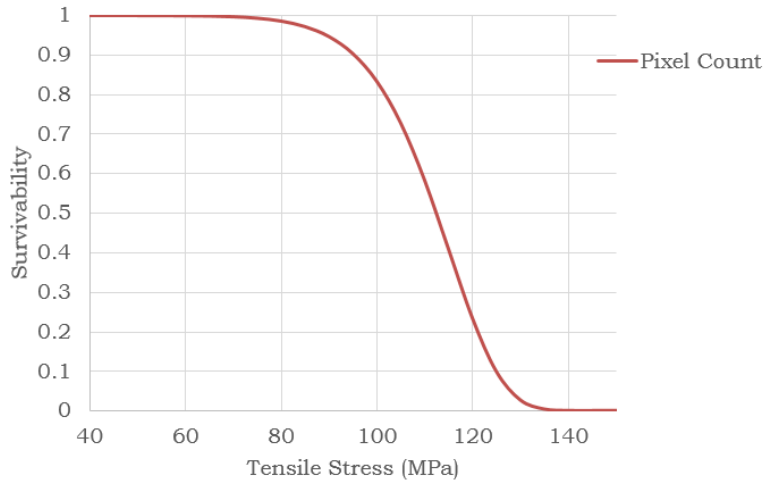

Figure C.2. Weibull survivability chart - analytically measured.

MICROMETER MEASURED

SUMMARY OUTPUT

Regression Statistics	
Multiple R	0.985015034
R Square	0.970254618
Adjusted R Square	0.966949576
Standard Error	0.22250626
Observations	11

ANOVA

	df	*SS*
Regression	1	14.53426747
Residual	9	0.445581323
Total	10	14.9798488

MS	*F*	*Significance F*
14.53426747	293.5679762	3.53607E-08
0.049509036		

	Coefficients	*Standard Error*		
Intercept	-45.42893161	2.620030125		
ln(tensile strength)	9.722020215	0.567416787		
t Stat	*P-value*	Beta	Alpha	
-17.33908751	3.1858E-08	9.722020215	106.9955451	
17.1338255	3.53607E-08			
Lower 95%	*Upper 95%*	*Lower 95.0%*	*Upper 95.0%*	
-51.35585152	-39.50201169	-51.35585152	-39.50201169	
8.438434265	11.00560616	8.438434265	11.00560616	

RESIDUAL OUTPUT

Observation	*Predicted ln(ln(1/(1-Median Rank))*	*Residuals*
1	-3.173730593	0.105857977
2	-2.04577648	0.125752689
3	-1.169006329	-0.186451952
4	-0.981938641	0.022198122
5	-0.408589698	-0.233687396
6	-0.357621514	-0.008891407
7	0.168946613	-0.281199856
8	0.287998021	-0.152477841
9	0.410192899	-0.017067249
10	0.499018069	0.190337013
11	0.692878498	0.4356299

Table C.1. Statistical regression of micrometer measured strength data.

PIXEL COUNT

SUMMARY OUTPUT

Regression Statistics	
Multiple R	0.967331898
R Square	0.935731001
Adjusted R Square	0.928590001
Standard Error	0.327064364
Observations	11

ANOVA

	df	*SS*
Regression	1	14.01710891
Residual	9	0.962739883
Total	10	14.9798488

MS	*F*	*Significance F*
14.01710891	131.0364123	1.14956E-06
0.106971098		

	Coefficients	*Standard Error*		
Intercept	-54.18012235	4.685852827		
ln(tensile strength)	11.39542937	0.995484946		
t Stat	*P-value*	Beta	Alpha	
-11.56248912	1.05586E-06	11.39542937	116.1112244	
11.44711371	1.14956E-06			
Lower 95%	*Upper 95%*	*Lower 95.0%*	*Upper 95.0%*	
-64.78025789	-43.57998682	-64.78025789	-43.57998682	
9.143485973	13.64737278	9.143485973	13.64737278	

RESIDUAL OUTPUT

Observation	*Predicted ln(ln(1/(1-Median Rank))*	*Residuals*
1	-3.192006294	0.124133679
2	-2.273244064	0.353220273
3	-0.806896116	-0.548562165
4	-0.68688397	-0.272856549
5	-0.352366899	-0.289910195
6	-0.182263708	-0.184249213
7	-0.127718173	0.01546493
8	0.205871699	-0.070351519
9	0.223036259	0.17008939
10	0.492700606	0.196654476
11	0.622141505	0.506366892

Table C.2. Statistical regression of analytically measured strength data.